1521-0103/347/1/145–153$25.00
THE JOURNAL OF PHARMACOLOGY AND EXPERIMENTAL THERAPEUTICS

http://dx.doi.org/10.1124/jpet.113.205138
J Pharmacol Exp Ther 347:145–153, October 2013

Enhancement of Ca^{2+} Influx and Ciliary Beating by Membrane Hyperpolarization due to ATP-Sensitive K^+ Channel Opening in Mouse Airway Epithelial Cells

Teruya Ohba, Eiji Sawada, Yoshiaki Suzuki, Hisao Yamamura, Susumu Ohya, Hiroyuki Tsuda, and Yuji Imaizumi

Department of Molecular and Cellular Pharmacology, Graduate School of Pharmaceutical Sciences (T.O., E.S., Y.S., H.Y., Y.I.) and Nanomaterial Toxicology Project (H.T.), Nagoya City University, Nagoya, Japan; and Department of Pharmacology, Division of Pathological Sciences, Kyoto Pharmaceutical University, Kyoto, Japan (S.O.)

Received March 25, 2013; accepted August 5, 2013

ABSTRACT

Among the several types of cells composing the airway epithelium, the ciliary cells are responsible for one of the most important defense mechanisms of the airway epithelium: the transport of inhaled particles back up into the throat by coordinated ciliary movement. Changes in the cytoplasmic Ca^{2+} concentration ($[Ca^{2+}]_i$) are the main driving force controlling the ciliary activity. In mouse ciliary cells, membrane hyperpolarization from −20 to −60 mV under whole-cell voltage-clamp induced a slow but significant $[Ca^{2+}]_i$ rise in a reversible manner. This rise was completely inhibited by the removal of Ca^{2+} from the extracellular solution. Application of diazoxide, an ATP-dependent K^+ channel opener, dose-dependently induced a membrane hyperpolarization (EC_{50} = 2.3 μM), which was prevented by the addition of 5 μM glibenclamide. An inwardly rectifying current was elicited by the application of 10 μM diazoxide and suppressed by subsequent addition of 5 μM glibenclamide. Moreover, the application of 10 μM diazoxide induced a significant $[Ca^{2+}]_i$ rise and facilitated ciliary movement. Multi-cell reverse-transcription polymerase chain reaction analyses and immunocytochemical staining suggested that the subunit combination of Kir6.2/SUR2B and possibly also Kir6.1/SUR2B is expressed in ciliary cells. The confocal Ca^{2+} imaging analyses suggested that the $[Ca^{2+}]_i$ rise induced by diazoxide occurred preferentially in the apical submembrane region. In conclusion, the application of a K_{ATP} channel opener to airway ciliary cells induces membrane hyperpolarization and thereby induces a $[Ca^{2+}]_i$ rise via the facilitation of Ca^{2+} influx through the non–voltage-dependent Ca^{2+} permeable channels. Therefore, a K_{ATP} opener may be beneficial in facilitating ciliary movement.

Introduction

The regulation of K^+ channel conductance is suggested to be a critical issue in the therapy of asthma and/or chronic obstructive pulmonary disease (Pelaia et al., 2002; Malerba et al., 2010). The activation of the ATP-sensitive K^+ (K_{ATP}) channel, the large conductance Ca^{2+}-activated K^+ (BK) channel, or the intermediate conductance Ca^{2+}-activated K^+ (IK) channel by specific modulators induces the following: bronchodilation, reduced airway hyperresponsiveness, reduced mucus production and cough, suppressed airway inflammation, and the remodeling of the preclinical models of asthma and chronic obstructive pulmonary disease (Malerba et al., 2010).

Ciliary cells play a fundamental role in the airway self-defense system by removing foreign materials from the airways in functional combinations with the other types of epithelial cells. The motile cilia in the airway epithelium are the engines for mucociliary clearance, which is a mechanism responsible for cleaning the airways of inhaled particles. The ciliary beating observed in the human airway epithelium is principally due to a slow constitutive rate of beating caused by inherent and spontaneous dynein ATPase activity. The cilia can increase their beating frequency by the activation of several different control mechanisms, one of these being changes in the intracellular Ca^{2+} concentration ($[Ca^{2+}]_i$) (Evans and Sanderson, 1999; Schmid and Salathe, 2011). Aside from the regulatory effects of calcium on the ciliary beating rate, calcium is also involved in the complex task of synchronizing the beat among the cilia of one single cell as well as between the cilia on multiple cells (Schmid and Salathe, 2011).

This investigation was supported by a Grant-in-Aid for Scientific Research on Priority Areas [Grant 23136512] (to Y.I.) from the Ministry of Education, Culture, Sports, Science, and Technology in Japan; and by a Grant-in-Aid for Scientific Research [Grant 23390020] (to Y.I.) from the Japan Society for the Promotion of Science. This work was also supported by Health and Labor Sciences Research grants from the Ministry of Health, Labor and Welfare, Japan [Research on Risk of Chemical Substance 21340601, H19-kagaku-ippan-006, and H22-kagaku-ippan-005] (to H.T.).
T.O. and E.S. contributed equally to this study.
dx.doi.org/10.1124/jpet.113.205138

ABBREVIATIONS: BK, large conductance Ca^{2+}-activated K^+ channel; $[Ca^{2+}]_i$, intracellular Ca^{2+} concentration; CBF, ciliary beating frequency; DPBS, Dulbecco's phosphate-buffered saline; fluo-4/AM, fluo-4 acetoxymethyl ester; fura-2/AM, fura-2 acetoxymethyl ester; K_{ATP} channel, ATP-sensitive K^+ channel; NGS, normal goat serum; PBS, phosphate-buffered saline; PCR, polymerase chain reaction; SUR, sulfonylurea receptor; VDCC, voltage-dependent Ca^{2+} channel.

Initially, K_{ATP} channels were identified as the key molecules for insulin secretion in pancreatic β-cells; they are now well known to be ubiquitously expressed in a variety of tissues as the molecular combination of channel-forming Kir6.x subunits and sulfonylurea receptors (SURs) (Clark and Proks, 2010; Flagg et al., 2010; Hibino et al., 2010). Although the expression of K_{ATP} channels has been reported in alveolar cells (Trinh et al., 2007) and cell lines derived from human airway epithelial tissues (Trinh et al., 2008), their functional expression in ciliary cells has not yet been documented. Previous studies have revealed that ATP and acetylcholine are major endogenous stimulants that facilitate ciliary beating by activating the purinoceptors and by increasing $[Ca^{2+}]_i$, which, in turn, may induce membrane hyperpolarization via the activation of Ca^{2+}-dependent K^+ channels (Weiss et al., 1992; Tarasiuk et al., 1995). However, conflicting reports have been published on whether changes in the membrane potential can significantly affect the ciliary beat frequency (Ma et al., 2002). Therefore, the present study was undertaken to elucidate the effects of K_{ATP} openers on ciliary beating rates and to determine the underlying mechanisms of the changes. The effects of K_{ATP} openers on ciliary beating may be a key issue in evaluating their therapeutic potentials for respiratory diseases.

Materials and Methods

Animals. C57BL/6N male mice (Japan SLC, Hamamatsu, Japan), 8 to 12 weeks old, were used. All experiments were carried out in accordance with the Guiding Principles for the Care and Use of Laboratory Animals of the Japanese Pharmacological Society and also with the approval of the Ethics Committee of Nagoya City University.

Isolation of Single Ciliary Cells. The tracheas were removed from the mice. The epithelium was separated from the cartilage and cut into squares of approximately 1 × 1 mm. The tissue was maintained in Dulbecco's phosphate-buffered saline (DPBS) containing (in mM): 137 NaCl, 2.7 KCl, 0.9 $CaCl_2$, 0.5 $MgCl_2$, 8 Na_2HPO_4, 1.47 KH_2PO_4, and 5 glucose, pH 7.4. The epithelium was incubated for 25 minutes at 37°C in DPBS supplemented with 13 U/ml papain (Sigma-Aldrich, St. Louis, MO), 1 mg/ml bovine serum albumin (Sigma-Aldrich), and 1 mg/ml 1,4-dithiothreitol (Wako Pure Chemicals, Osaka, Japan). After incubation, the solution was replaced with DPBS. The cells were then dispersed several times with a fire-polished Pasteur pipette. The isolated cells were immediately used following the cell dispersion. All of the experiments were carried out at room temperature (25°C).

Multicell Reverse-Transcription Polymerase Chain Reaction. Approximately 40 ciliary cells were collected by the glass electrode of ~2-30 μm in diameter. Total RNA was extracted from them using NucleoSpin RNA XS (Macherey Nagel, Düren, Germany) and reverse-transcribed using oligo$(dT)_{12-18}$ primer and SuperScript II reverse transcriptase (Invitrogen, Carlsbad, CA). The solution without RTase was used as a negative control. The polymerase chain reaction (PCR) amplification profile using KOD-Plus-Neo (TOYOBO, Tokyo, Japan) and GeneAmp PCR System 2700 (Applied Biosystems, Foster City, CA) was as follows: a 10-second denaturation step at 98°C, a 30-second annealing step at 55°C, and a 60-second primer extension step at 72°C for 35 cycles. Gene products were analyzed by 2.0% agarose gel electrophoresis.

PCR Primers. The following PCR primers were used: for mouse Kir6.1/Kcnj8 (GenBank Accession No. NM_008428), (+) 5′-CAA GTG ACC ATT GGG TTT GGA-3′ and (−) 5′-CGT TGA TGA TCA GAC CCA CGA-3′ (100 bp); Kir6.2/Kcnj11 (NM_010602), (+) 5′-CAA GAA AGG CAA CTG CAA CGT-3′ and (−) 5′-TGT GTG GCC ATT TGA GGT CCA-3′ (101 bp); SUR1/Abcc8 (NM_011510), (+) 5′-AGT GAA GCC CCC TGA GGA CCT-3′ and (−) 5′-GAT GAA GGC ATT CAT CCA CCA-3′ (103 bp); SUR2/Abcc9 (NM_021041 and NM_011511), (+) 5′-TAC GAA CAT CAT CGA CCA GCA-3′ and (−) 5′-AAA CAC GGG TGT AGC ATA GGA-3′ (109 bp); β-actin/Actb (NM_007393), 5′-AGG CCA ACC GTG AAA AGA TG-3′ and (−) 5′-ACC AGA GGC ATA CAG GGA CA-3′ (101 bp). The specific primers for the spliced variant analysis of SUR2 were designed as follows: for mouse SUR2A/Abcc9A (NM_021041), (+) 5′-TCT TCT ATT GTG GAT GCA GGC CT-3′ and (−) 5′-CTA CTT GTT GGT CAT CAC CAA AGT-3′ (129 bp); SUR2B/Abcc9B (NM_011511), (+) 5′-CAC ACC ATT CTG ACT GCA GAC CT-3′ and (−) 5′-TCA CAT GTC TGC ACG GAC AAA CGA-3′ (129 bp).

Immunocytochemistry. Polyclonal antimouse Kir6.2 (APC-020) and control antigen were purchased from Alomone Laboratories (Jerusalem, Israel). Polyclonal antibodies to Kir6.1 (R-14), SUR1 (H-80), SUR2A (M-19), SUR2B (C-15) and each blocking peptide were purchased from Santa Cruz Biotechnology, Inc. (Dallas, TX). Dissociated ciliary cells were settled down on coverslips precoated with poly-L-lysine (Matsunami Glass Industry, Osaka, Japan). These cells were fixed with 4% paraformaldehyde for 20 minutes and permeabilized with 0.2% Triton/phosphate-buffered saline (PBS) for 15 minutes at room temperature. After rinsing in PBS containing 1% normal goat serum (NGS), the cells were preincubated for 1 hour with 10% NGS/PBS to minimize nonspecific binding of antibodie, and incubated successively with 1:100 diluted antibodies for 12 hours. Primary antibodies were extensively washed with 1% NGS/PBS and incubated with Alexa 488-conjugated antirabbit IgG goat or Alexa 488-conjugated antigoat IgG rabbit antiserum (Molecular Probe, Eugene, OR) for 1 hour. Immunostained cells were observed using an A1R laser-scanning confocal fluorescent microscope (Nikon, Tokyo, Japan) equipped with a fluorescent microscope (ECLIPSE Ti; Nikon), an objective lens (Plan Apo 60× 1.40 NA oil immersion; Nikon), and NIS Elements software (version 3.10; Nikon). The excitation wavelength from the multiargon laser (Melles Griot, Carlsbad, CA) for Alexa 488 was 488 nm, and the emission light was collected by a band-pass filter (525/50 nm).

Electrophysiological Recordings. A whole-cell patch clamp was applied to a single ciliary cell with a patch pipette using a CEZ-2400 amplifier (Nihon Kohden, Tokyo, Japan) as previously described (Imaizumi et al., 1989; Yamamura et al., 2012). The membrane currents and voltage signals were stored and analyzed using a Digidata 1440A and a pCLAMP 10.2 (Axon Instruments, Foster City, CA). The ciliary cells were clamped at a holding potential of −40 mV, and a descending ramp protocol from +40 to −120 mV for 500 milliseconds was performed every 10 seconds. In some experiments, membrane potentials from single ciliary cells were measured under the current-clamp mode in whole-cell configuration.

Measurement of the Ca^{2+} Fluorescence Ratio and the Ca^{2+} Images. The airway ciliary cells were loaded with 10 μM fura-2 acetoxymethyl ester (fura-2/AM; Molecular Probes) in a standard HEPES solution for 45 minutes at room temperature. The fura-2 fluorescent signals were measured using the Argus/HiSCA imaging system (Hamamatsu Photonics, Hamamatsu, Japan). In some experiments, in which simultaneous measurements of $[Ca^{2+}]_i$ and membrane potential were taken, ciliary cells were loaded with 100 μM fluo-4 (Molecular Probes) by diffusion from the recording pipette (Funabashi et al., 2010). The Ca^{2+} images were scanned every 2 seconds.

Intracellular Ca^{2+} Images by Use of Fluo-4/AM and Confocal Fluorescent Microscopy. The airway ciliary cells were loaded with 10 μM fluo-4 acetoxymethyl ester (fluo-4/AM; Molecular Probes) in a standard HEPES solution for 45 minutes at room temperature. The cytosolic Ca^{2+} images were obtained using the aforementioned laser-scanning confocal fluorescent microscope and NIS Elements software. The excitation wavelength for fluo-4 was 488 nm, and the emission wavelength was collected by a bandpass filter (525/50 nm). The resolution of the microscope was 0.414 μm per pixel and 2.02 μm to the Z-axis direction. The confocal images were scanned over a full frame (512 × 512 pixels) every 2 seconds.

Membrane Potential Measurements by Voltage-Sensitive Fluorescent Dye. The membrane potential was measured as previously reported (Yamazaki et al., 2011) using 100 nM $DiBAC_4(3)$ (Dojin,

Kumamoto, Japan), a bis-barbituric acid oxonol dye with an excitation maximum at approximately 488 nm. The data were collected and analyzed using the Argus/HiSCA imaging system. The sampling interval of the $DiBAC_4(3)$ fluorescence measurements was every 5 seconds.

Measurement of Ciliary Beating Frequency. The ciliary beating frequency (CBF) of the tracheal airway ciliary cell (Shiima-Kinoshita et al., 2004; Kawakami et al., 2004) was measured at 100 Hz using a high-speed resolution CCD camera (C9100-12, Hamamatsu Photonics). Prior to the experiments, the CBFs were measured every 1 minute for 2 minutes, and the average value of these three CBFs were used as the basal CBF (CBF_0) in the HEPES-buffered solution. Any changes in the CBF were expressed as a CBF ratio.

Solutions. An extracellular solution was made using a standard HEPES-buffered solution composed of the following (in mM): 137 NaCl, 5.9 KCl, 2.2 $CaCl_2$, 1.2 $MgCl_2$, 14 glucose, and 10 HEPES. The pH of the solution was adjusted with NaOH to 7.4. The K_{ATP} current was measured in a 40 mM K^+ HEPES-buffered solution composed of the following (in mM): 99.7 NaCl, 40 KCl, 2.2 $CaCl_2$, 1.2 $MgCl_2$, 14 glucose, and 10 HEPES. The pH of the solution was adjusted with NaOH to 7.4. The pipette solution for electrical recordings contained the following (in mM): 140 KCl, 4 $MgCl_2$, 2 ATP-Na_2, 0.05 EGTA, 10 HEPES. The pH of the solution was adjusted with KOH to 7.2. All experiments were undertaken at room temperature to avoid fura-2 trapping in organelles and dye leakage at 37°C.

Statistical Analysis. The pooled data are expressed as means ± S.E., and the statistical significance was examined using Student's t test for two groups and Tukey's for three or more groups. P values < 0.05 were considered statistically significant. The data of the relationship between diazoxide and fluorescent signal were fitted using the following equation after normalization: $F/F_0 = 1 - (1 - C)/\{1 + (K_d/[\text{diazoxide}])^n\}$, where C is the component resistant, K_d is the apparent dissociation constant, [diazoxide] is the concentration, and n is the Hill coefficient (Fig. 2D).

Drugs. The pharmacological reagents were obtained from Sigma-Aldrich. Diazoxide, glibenclamide, and pinacidil were dissolved in dimethylsulfoxide at concentrations of 5 to 10 mM as a stock solution.

Results

The Effects of K_{ATP} Opener on Ciliary Beating. The ciliary movement in freshly isolated mice ciliary cells was recorded at 100 Hz using a high time-resolution video camera and analyzed using a slow image reproduction (Fig. 1A). The application of 10 μM diazoxide, a K_{ATP} channel opener, significantly increased the frequency of the ciliary movement (Fig. 1B), and the effect lasted for over 10 minutes (not shown). The addition of 5 μM glibenclamide, a K_{ATP} channel blocker, removed the diazoxide-induced enhancement of the frequency (Fig. 1B). The summarized data (Fig. 1C) indicate a significant enhancement of the frequency when 10 μM diazoxide was applied ($n = 6$, $P < 0.05$ versus control) and a significant inhibition of the frequency when 5 μM glibenclamide was added ($n = 6$, $P < 0.01$ versus diazoxide alone). Although the amplitude of the movement may also be increased by the diazoxide, those quantitative analyses could not be done during this study due to the limited time resolution of the video system.

The K_{ATP} Opener–Induced Membrane Hyperpolarization and the Subsequent Rise in $[Ca^{2+}]_i$. The membrane potential changes induced by the addition of 10 μM diazoxide in the isolated ciliary cells were measured using the voltage sensitive fluorescent dye $DiBAC_4(3)$.

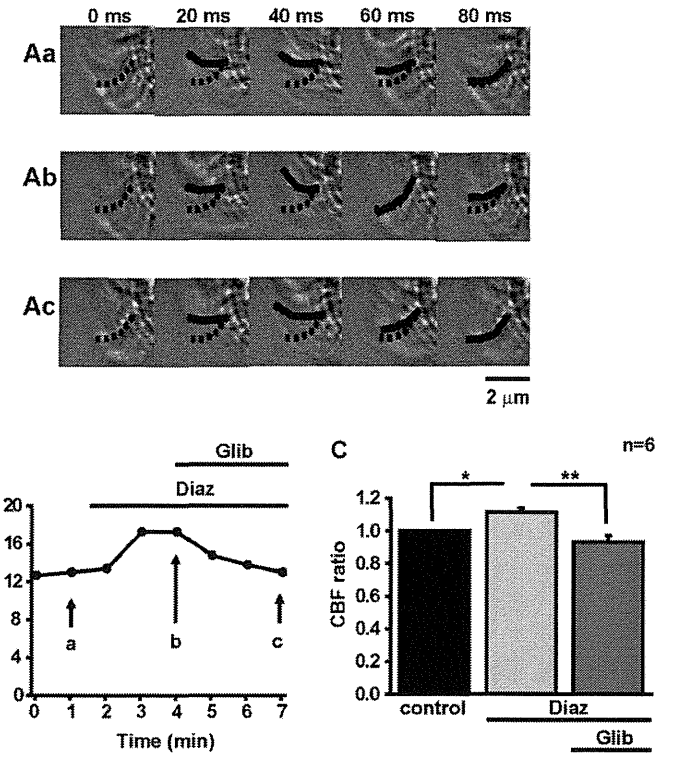

Fig. 1. The enhancement of the ciliary movement by diazoxide. (A) The ciliary movement in an epithelial cell isolated from a mouse trachea was recorded with a high-speed digital camera at 100 Hz. The CBF was directly measured from the images as shown by the dotted and solid lines. The series of images (a, b, and c) were obtained at the time shown in B. (B) The time course of CBF in HEPES-buffered solution, in the presence of 10 μM diazoxide (Diaz), and following the addition of 5 μM glibenclamide (Glib). (C) The summarized data concerning the effects of diazoxide and glibenclamide ($n = 6$). *,**$P < 0.05$ and 0.01, respectively.

The sustained decrease in the fluorescence intensity observed following the addition of 10 μM diazoxide is indicative of membrane hyperpolarization ($n = 5$, $P < 0.01$). The diazoxide-induced decrease in fluorescence intensity was completely removed by the addition of 5 μM glibenclamide ($n = 5$, $P < 0.01$; Fig. 2, A and B). The diazoxide-induced decrease in fluorescence intensity was concentration-dependent in the range of 1 and 30 μM (Fig. 2, C and D). The EC_{50} value for membrane potential of the cells treated with diazoxide was 2.3 μM, and the Hill coefficient was 3.4 ($n = 11$).

The membrane potential was also measured under current-clamp mode in freshly isolated single ciliary cells using pipette filling solution containing 140 mM KCl (see *Materials and Methods*). In all four experiments, stable recordings for over 10 minutes were successfully obtained throughout the procedure of adding two drugs sequentially; the addition of 10 μM diazoxide induced sustained membrane hyperpolarization of 3.6 ± 1.4 mV from the resting membrane potential of −18.6 ± 1.4 mV ($n = 4$). Further addition of 5 μM glibenclamide resulted in depolarization by 2.4 ± 0.5 mV ($n = 4$). Taking the initial resting membrane potential in each cell as 1.0, the potentials after the addition of diazoxide and glibenclamide were 1.20 ± 0.03 ($P < 0.01$ versus 1.0) and 1.07 ± 0.03 ($P < 0.05$ versus diazoxide alone).

The effects of the diazoxide on $[Ca^{2+}]_i$ were examined in isolated ciliary cells using fura-2/AM (Fig. 3). The application of 10 μM diazoxide increased the fluorescence ratio (F340/F380), indicating the increase in $[Ca^{2+}]_i$ ($n = 8$, $P < 0.01$). This

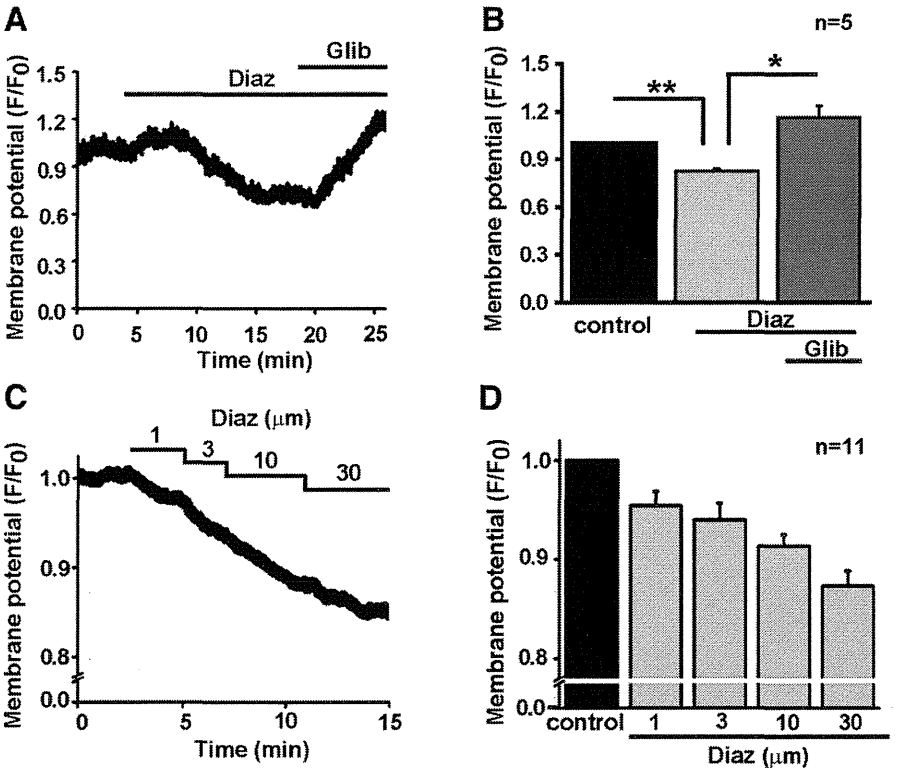

Fig. 2. The diazoxide-induced hyperpolarization of the membrane. (A) The changes in the membrane potential were monitored by the voltage-sensitive dye $DiBAC_4(3)$. The changes in the fluorescent intensity ratio (F/F_0) that were induced by the addition of 10 μM diazoxide (Diaz) and 5 μM glibenclamide (Glib) were plotted against time. The average fluorescent intensity (F) measured immediately prior to the application of the diazoxide was taken as F_0. (B) The summarized data concerning F/F_0 are shown (n = 5). *,**$P < 0.05$ and 0.01, respectively. (C) The changes in F/F_0 that were induced by the cumulative additions of diazoxide in a dose range from 1 to 30 μM were plotted against time. (D) The summarized data concerning F/F_0 are shown (n = 11). The EC_{50} value and Hill coefficient were 2.3 and 3.4 μM, respectively.

observed increase was removed by the addition of 5 μM glibenclamide (n = 8, $P < 0.01$). The $[Ca^{2+}]_i$ was also increased by the application of 10 μM pinacidil, another K_{ATP} channel opener (n = 5, $P < 0.01$), and the effect was again reversed by the addition of 5 μM glibenclamide (n = 5, $P <$ 0.01).

The Expression of ATP-Sensitive K^+ Channels in Ciliary Cells. The molecular characteristics of the K_{ATP} channels in the ciliary cells were examined by multicell reverse-transcription PCR analysis. These analyses reveal that the transcripts of Kir6.2 and SUR2B were predominantly expressed in the ciliary cells (n = 3; Fig. 4A).

To clarify protein expression of these channels, immunocytochemical analyses were performed (n = 3; Fig. 4B). Kir6.1, Kir6.2 and SUR2B proteins were detected on plasma membrane of ciliary cells. However, SUR2A did not show significant membrane surface expression. These results are consistent with those from reverse-transcription PCR analyses and strongly suggest that Kir6.2/SUR2B and possibly also Kir6.1/SUR2B are predominantly expressed in mouse ciliary cells. We did not expect to find that SUR1 showed specific expression on cilia.

The Measurement of ATP-Sensitive K^+ Channel Currents in Ciliary Cells. The K_{ATP} channel current was measured in a single ciliary cell using a whole-cell patch-clamp recording. To amplify the conductance of the Kir channel, the recordings were performed in an external solution containing 40 mM K^+. The current–voltage relationship in the control showed slight inward rectification at potentials negative to −60 mV. The inwardly rectifying current was markedly enhanced by the application of 10 μM diazoxide (Fig. 5A). The enhanced current was reduced by the addition of 5 μM glibenclamide. The reversal potential of the current component reduced by glibenclamide in the presence of diazoxide was −33 mV, which is close to the equilibrium potential of K^+ under the conditions (E_K = −32 mV). The summarized data (Fig. 5B) clearly indicate that the inward K^+ current density at −110 mV was significantly enhanced by the application of diazoxide (n = 7, $P < 0.05$ versus control) and markedly reduced by the addition of glibenclamide (n = 5; $P < 0.05$ versus diazoxide alone).

The Relationship between the Membrane Potential and $[Ca^{2+}]_i$ in the Isolated Ciliary Cells. The relationship between the membrane potential and $[Ca^{2+}]_i$ was determined in isolated ciliary cells under a whole-cell voltage-clamp. The single ciliary cells were loaded with fluo-4 from recording pipettes. A membrane hyperpolarization from −20 to −60 mV induced a slow increase in $[Ca^{2+}]_i$ (n = 4, $P < 0.01$) and the return of the potential to −20 mV removed the increase in $[Ca^{2+}]_i$ completely but at a much slower rate (n = 4, $P < 0.05$; Fig. 6, A and B). The $[Ca^{2+}]_i$ increase induced by hyperpolarization was also abolished by the withdrawal of 2.2 mM Ca^{2+} in the external solution (n = 3, $P < 0.01$; Fig. 6, C and D). As shown in Fig. 6, the time courses of $[Ca^{2+}]_i$ elevation varied widely from cell to cell, presumably due to the diversity of cell activities after isolation and also the difference in the load of Ca^{2+} indicator among cells. The summarized data indicate that the $[Ca^{2+}]_i$ increase induced by hyperpolarization from −20 to −60 mV was significant, reversible, and susceptible to external Ca^{2+}.

The Image Analyses of Local $[Ca^{2+}]_i$ Changes by Diazoxide in the Ciliary Cells. The image analyses of changes in the local $[Ca^{2+}]_i$ were performed using fluo-4/AM and a confocal fluorescent microscope. The changes in the fluorescent intensity of the three areas in the ciliated cell (central, apical, and basolateral areas indicated by "a," "b," and "c," respectively, in Fig. 7A) by the application of 10 μM

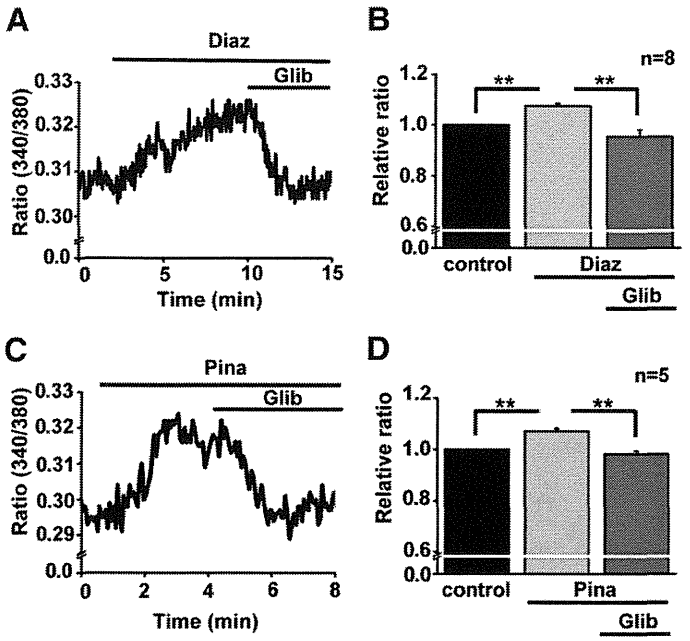

Fig. 3. The effects of diazoxide and glibenclamide on $[Ca^{2+}]_i$ in ciliated cells. (A) $[Ca^{2+}]_i$ was measured as fluorescent intensity ratio (*340/380*) in a ciliated cell that was loaded with fura-2/AM. The changes in the ratio induced by the addition of 10 μM diazoxide (Diaz) and 5 μM glibenclamide (Glib) were plotted against time. (B) The summarized data concerning the changes in F/F_0 are shown (n = 8). The averaged ratio immediately prior to the application of diazoxide was taken as 1.0. $^{**}P < 0.01$. (C) The changes in the ratio induced by the addition of 10 μM pinacidil (Pina) and 5 μM glibenclamide (Glib) were plotted against time. (D) The summarized data concerning the changes in F/F_0 are shown (n = 5). The averaged ratio immediately prior to the application of the pinacidil was taken as 1.0. $^{**}P < 0.01$.

diazoxide over time were illustrated in Fig. 7B. When the intensity at resting conditions in the cell center was taken as unity, the intensities at the apical area and the basolateral area were 1.01 ± 0.01 and 1.00 ± 0.02, respectively ($n = 9, P >$ 0.05 among the three areas). After the application of 10 μM diazoxide, the intensities in each area gradually increased (Fig. 7, A and B). The rise in intensity at the apical area was more focal, faster, and larger than the rise in intensity at either the cell center or the basolateral area (Fig. 7C). The summarized data (Fig. 7D) indicate that the rise in intensity at the cell center was significantly less than the rise in intensity at the apical area ($n = 9, P < 0.05$). The rise in intensity at the basolateral area tended to be smaller than the rise in intensity at the apical area, but the difference was not significant.

In addition to the focal rise in submembrane area of the apical side (Fig. 7C, ii and iii), Ca^{2+} rise in the cytosol compartments located deep inside the cell was occasionally observed (Fig. 7C, iii, iv, and v). This type of Ca^{2+} rise was characteristic of a slow rise, deep-inside location, and nonfocal or diffused images. This specific rise was observed to varying degrees in seven of nine cells, whereas the focal and rapid Ca^{2+} rises in the apical submembrane areas were clearly detected in all nine cells examined.

Discussion

Ca^{2+} as One of the Major Factors Modulating Mucociliary Motility. In the ciliary mechanism, the basic mechanism that is responsible for the slow and constitutive rate of beating is considered to be the inherent and spontaneous dynein ATPase activity that depends mainly upon the cellular MgATP concentration (Salathe and Bookman, 1999; Ma et al., 2002). In addition, adapting to the heavier duty of particle transportation with mucus in the epithelium, the upregulation of the ciliary motility by three separate second messengers have been clarified: Ca^{2+}, c-AMP, and c-GMP (Salathe, 2007). The cross-talk among signal pathways by these three second messengers has been also revealed. Among these second messengers, Ca^{2+} has fundamental roles in facilitating CBF (Schmid and Salathe, 2011). The application of a K_{ATP} opener increases the CBF by only 10–15% above the baseline in airway ciliated cells. It has been demonstrated, however, that a 16% increase in CBF results in 56% increase in the mucociliary transport velocity in an isolated trachea (Seybold et al., 1990). In this study, the maximum response to the externally applied physiologic stimulants ATP or acetylcholine often resulted in larger rises in $[Ca^{2+}]_i$ than those induced by K_{ATP} openers. These slightly larger increases in CBF (15–30%) suggest that mucociliary clearance may therefore be substantially enhanced by K_{ATP} channel openers.

New Insight into $[Ca^{2+}]_i$ Regulation by the Membrane Potential Changes in Airway Ciliated Cells. Information concerning the influence of changes in the membrane potential on the ciliary axoneme movement is not well accumulated and still somewhat controversial. It has been reported that the application of ATP induces a $[Ca^{2+}]_i$ rise, leading to membrane hyperpolarization and facilitates the ciliary motility in frog palate and esophagus ciliated cells (Tarasiuk et al., 1995). In contrast, it has been reported that the membrane potential changes under the whole-cell voltage clamp mode does not induce a significant change in the single-airway ciliated cells of the rabbit (Ma et al., 2002). The findings in the present study clearly demonstrated that the membrane hyperpolarization achieved under a voltage clamp or induced by K_{ATP} channel openers elicited $[Ca^{2+}]_i$ rise and resulted in enhanced ciliary axoneme motility in the airway ciliated cells of the mice. The reason for the discrepancy between the studies in rabbit airway ciliated cells (Ma et al., 2002) and our results in mice is not completely clear. The changes in $[Ca^{2+}]_i$ by membrane hyperpolarization under whole-cell voltage-clamp were not recorded in the former study, presumably because the $[Ca^{2+}]_i$ was fixed by Ca^{2+}-EGTA buffer from the pipette filling solution (Ma et al., 2002). In the present study, the pipette solution contained only 50 μM EGTA and no $CaCl_2$, and the $[Ca^{2+}]_i$ rise by hyperpolarization was consistent and reversible. It is a rather common observation that prolonged membrane hyperpolarization induces a slow but sustained $[Ca^{2+}]_i$ rise in nonexcitable cells, such as T cells, chondrocytes (Funabashi et al., 2010), and vascular endothelial cells (Yamazaki et al., 2011) where the Ca^{2+} permeable channels are functionally expressed but the voltage-gated Ca^{2+} channels are not.

This study differs from the previous, conflicting study (Ma et al., 2002) based on the ATP concentrations used for experimentation. The previous study was conducted using 5 mM MgATP + 0.5 mM K_2ATP, whereas the current study was conducted using 4 mM $MgCl_2$ + 2 mM Na_2ATP. Although the basic CBF of inherent and spontaneous beating is considered to be dependent on MgATPase activity, the actual MgATP and ATP concentrations in the airway ciliated cells are unknown. It may be possible that experimental conditions in the present study influenced the CBF increase that were

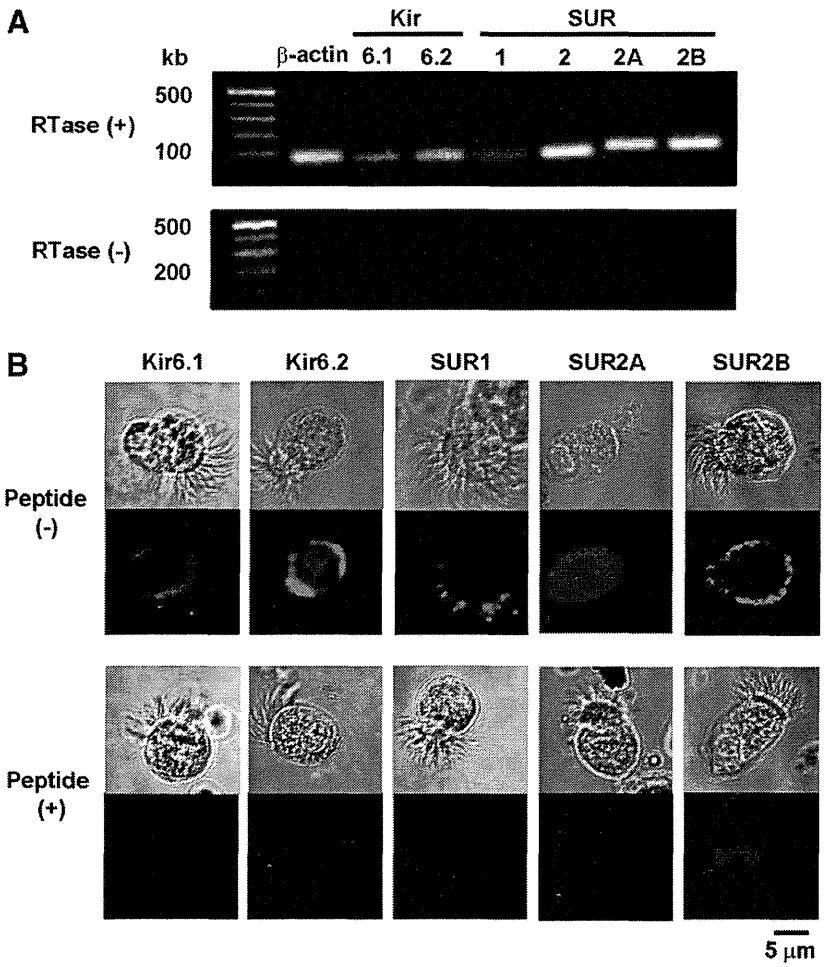

Fig. 4. The expression of K_{ATP} channel mRNA and protein in the ciliated cells. (A) The expression of Kir6.x and SURx in the ciliated cells was examined by multi-cell reverse-transcription PCR. Approximately 40 of the isolated ciliated cells in which ciliary movement was detected were collected by small pipettes in microscopic fields. Reaction solution from which RTase was omitted was used as a negative control. The expression of the transcripts for Kir6.1, Kir6.2 and SUR2 was detected. Further analyses suggest that the major transcript of SUR2 was SUR2B. (B) The protein expression was detected using immunocytochemical staining. Similarly to the results from RT-PCR, Kir6.1, Kir6.2, and SUR2B but not SUR2A were expressed on cell surface. SUR1 exhibited specific expression on cilia. The lower sets of panels indicate that the specific staining was prevented by a corresponding inhibitory peptide.

attributed to $[Ca^{2+}]_i$ rise by membrane hyperpolarization induced under voltage-clamp or by application of a K_{ATP} channel opener.

Previous studies have confirmed that the rise of $[Ca^{2+}]_i$ results in CBF enhancement, even if the underlying mechanisms are not fully understood (Schmid and Salathe, 2011). The activation of calmodulin may be involved, as this messenger protein associates with the radial spokes and the central apparatus of the flagella (Dymek and Smith, 2007) and directly interacts with dynein arms (Sakato et al., 2007). These mechanisms have been suggested for correlating the $[Ca^{2+}]_i$ rise with facilitated axoneme motility in invertebrates. In addition, it has been assumed that the $[Ca^{2+}]_i$ rise facilitates cilia motility via crosstalk with the cAMP or the cGMP mediated pathways (Braiman and Priel, 2008).

Ca^{2+} Source and Local Ca^{2+} Functions in the Regulation of Cilia Motility. In airway ciliated cells, it has been well established that two major endogenous stimulants, ATP and acetylcholine, activate P_2Y_2 and M_3 receptors, respectively. The stimuli activates phospholipase Cβ to form inositol 1,4,5 trisphosphate, which induces $[Ca^{2+}]_i$ release from the endoplasmic reticulum. In addition, sustained Ca^{2+} influx has been found to occur after Ca^{2+} release. Although the molecular mechanism of the Ca^{2+} influx is not well understood, the store-operated or receptor-operated Ca^{2+} entry may be contributing as it does in many other non-excitable cells. By some stimuli, such as stretch, the transient receptor potential vanilloid subfamily 4 (TRPV4) channel is activated to facilitate Ca^{2+} influx (Lorenzo et al., 2008).

In the present study, membrane hyperpolarization by voltage-clamp or the application of a K_{ATP} channel opener has been clearly shown to facilitate the influx of Ca^{2+}. Because airway epithelial cells are polarized structures with cilia on their apical membranes, Ca^{2+} concentrations are sufficiently high in the submembranous areas to affect ciliary beat (Braiman and Priel, 2008). It has been suggested that storage and release of Ca^{2+} in different cell compartments give rise to this apical versus basolateral concentration difference in the cytosol (Braiman et al., 2000; Braiman and Priel, 2001). In contrast, the measurement of the local $[Ca^{2+}]_i$ in this study did not show a significant Ca^{2+} gradient in the cytosol under the normal conditions (not shown). During membrane hyperpolarization by K_{ATP} openers, the Ca^{2+} rise in the apical submembrane area was significantly higher than that in the center area but not in the basolateral area.

In addition to a Ca^{2+} rise in the apical region, diazoxide occasionally induced a slower Ca^{2+} rise in the cytosolic compartments located deep inside the cells. Diazoxide reportedly interacts with the mitochondrial K_{ATP} channels as well as with plasma membrane K_{ATP} channels (Garlid et al., 1996; O'Rourke, 2004). Diazoxide reduces the mitochondrial membrane potential (or induces the mitochondrial depolarization) and thereby accelerates the release of Ca^{2+} from mitochondria (Grimmsmann and Rustenbeck, 1998; Holmuhamedov

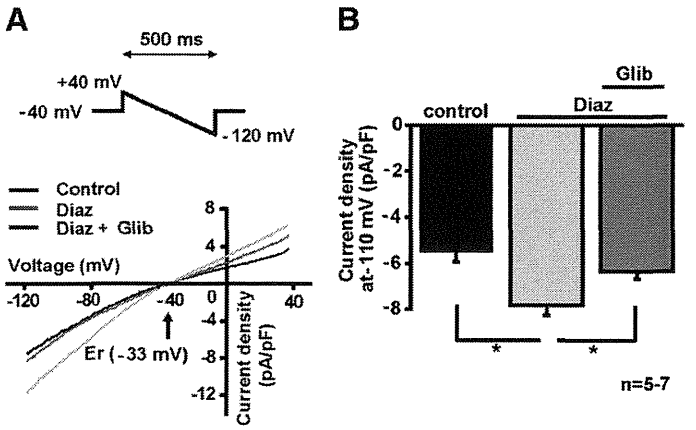

Fig. 5. K_{ATP} current in ciliated cells. (A) The membrane currents were measured from a single ciliary cell under a voltage-clamp. A ramp pulse from +40 to −120 mV (as indicated in inset) was applied in the absence (control) and the presence of 10 μM diazoxide (Diaz) and following the addition of 5 μM glibenclamide (Glib). The I-V relationships were obtained by the ramp pulse protocol. The I-V relationships in the presence of diazoxide with the absence and presence of glibenclamide crossed at −33 mV. (B) The data concerning the current density at −110 mV were summarized. The numbers of experiments were seven in the control, seven in the presence of diazoxide, and five in the co-presence of glibenclamide. *$P < 0.05$.

et al., 1999). In addition to the Ca^{2+} influx mediated by the membrane hyperpolarization, the release of Ca^{2+} from organelles, including mitochondria, may be involved in the diazoxide-induced Ca^{2+} increase. However, it remains to be determined whether the Ca^{2+} rise induced by diazoxide deep inside the cell compartments contributes to the enhancement of the ciliary movement. Further experiments are therefore required to elucidate the mechanism underlying the local Ca^{2+} mobilization triggered by exposure to diazoxide.

K_{ATP} Channels in Ciliated Cells as a Possible Therapeutic Target. K^+ channels play a major role in maintaining the electrochemical gradient necessary for transepithelial Na^+ and Cl^- transport in secretory airway epithelia (O'Grady and Lee, 2003). The K_{ATP} channel is believed to be a significant contributor to lung physiology and pathophysiology because of the beneficial actions of openers in the lung (Fukuse et al., 2002). The molecular components of the K_{ATP} channel in the airway alveolar epithelial type II cells of the rat have been identified as the combination of Kir6.1 and SUR2B (Leroy et al., 2004). A K_{ATP} channel opener induces the relaxation of airway smooth muscle via membrane hyperpolarization and the subsequent suppression of voltage-dependent Ca^{2+} channel (VDCC) activity (Rodrigo and Standen, 2005). This relaxation is considered to be effective for the therapy of occlusive diseases, such as asthma and chronic obstructive pulmonary disease (Pelaia et al., 2002).

In this study, two K_{ATP} channel openers, diazoxide and pinacidil, and the K_{ATP} channel blocker glibenclamide were used as pharmacological tools to determine the subunits responsible for K_{ATP} channel activation in mouse ciliated cells. The combination of K_{ATP} channel subunits modulates sensitivity to K_{ATP} channel openers. Diazoxide activates SUR1 and SUR2B but not SUR2A (Yamada and Kurachi, 2005). On the other hand, pinacidil activates SUR2A and SUR2B but not SUR1. Because K_{ATP} channels in ciliated cells were activated by both diazoxide and pinacidil at <10 μM, functional K_{ATP} channels in these cells are supposed to be Kir6.x/SUR2B (Hibino et al., 2010). These results were supported by the outcomes from reverse-transcription PCR analyses and immunocytochemical staining, which showed the expression of Kir6.1, Kir6.2, and SUR2B on plasma membrane. It is interesting that immunostaining using anti-SUR1 revealed that SUR1 subunits were specifically located on cilia, but neither Kir6.1 nor Kir6.2 was detected there. SUR1 may possibly couple with other ion channels, such as the transient receptor potential channel (Woo et al., 2013). Unfortunately, the strategy of molecular manipulation by use of siRNA did not fit to this study because rat cilia disappear during cell culture for 2 days (Chang et al., 1985); the results were

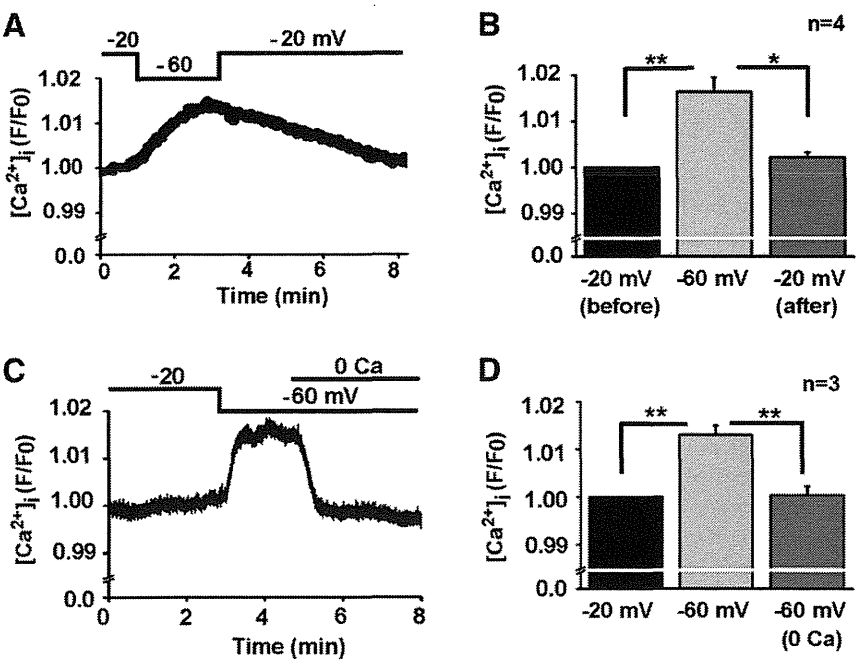

Fig. 6. $[Ca^{2+}]_i$ changes induced by the membrane hyperpolarization in ciliary the cells under a voltage-clamp. (A) The changes in $[Ca^{2+}]_i$ were monitored with the F/F_0 of the fluo4 that was applied from the recording pipette. The time course of F/F_0 during the membrane potential changes from −20 mV to −60 mV and back to −20 mV was plotted against time. The top trace indicates the clamp potential changes. (B) The summarized data concerning F/F_0 at −20 mV, at −60 mV, and back to −20 mV are shown ($n = 4$). *,**$P <$ 0.05 and 0.01, respectively. (C) The effect of Ca^{2+} removal from an external solution on the elevated F/F_0 by the hyperpolarization of the membrane was examined in a ciliary cell under a voltage clamp. The external solution was exchanged from the standard solution (2.2 mM Ca^{2+}) to a Ca^{2+} free solution (0 mM Ca^{2+}) at a potential of −60 mV as indicated in the top trace. (D) The summarized data concerning F/F_0 at −20 mV at −60 mV and following the exposure to a Ca^{2+} free solution are shown ($n = 4$). *,**$P < 0.05$ and 0.01, respectively.

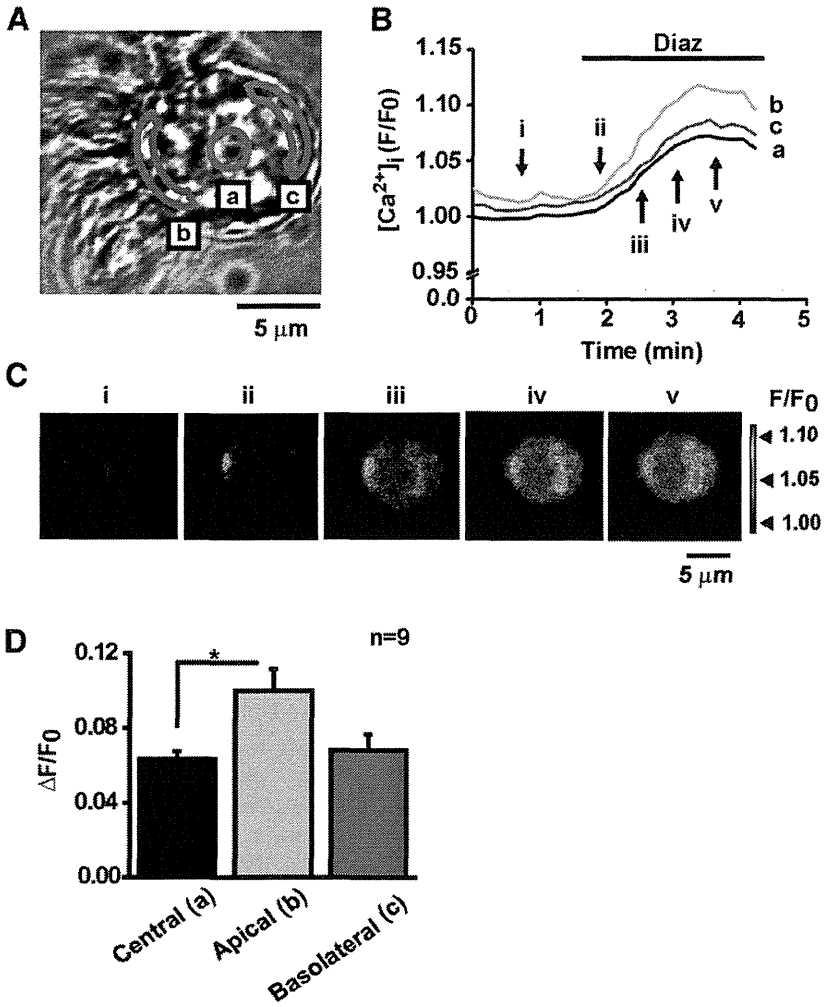

Fig. 7. The image analyses of local Ca^{2+} transients induced by diazoxide in the ciliary cells. (A) The local Ca^{2+} transients were measured by confocal fluorescent microscopy. The F/F_0 signals of fluo-4 were measured in the three areas indicated in the transfer image of the ciliary cell: "a" (center of the cell). "b" (apical submembrane area), and "c" (basolateral submembrane area). (B) Changes in F/F_0 in the three areas were plotted against time. The F_0 in area "a" was taken as 1.0 and F/F_0 in the other areas was normalized by the F_0. (C) The confocal images of $[Ca^{2+}]_i$ were obtained from the ciliary cell in the absence (i) and presence (ii, iii, and iv) of diazoxide at the timing shown in B. (D) The summarized data concerning $\Delta F/F_0$ were obtained as the differences of F/F_0 in the absence and presence of diazoxide in B ($n = 9$). $^*P < 0.05$.

confirmed using mouse cilia in this study. Therefore, it remains to be determined whether Kir6.1 or Kir6.2 is the functionally predominant subunit in ciliated cells, whereas Kir6.2 protein expression on the plasma membrane appeared to be higher than Kir6.1.

Membrane potential recording with $DiBAC_4(3)$ allows us to get more number of results than the direct recordings under whole-cell patch clamp configuration. However, the use of $DiBAC_4(3)$ has at least three limitations. First, the artifacts by $DiBAC_4(3)$ act as a potent activator of BK channel (Morimoto et al., 2007). BK channel current component sensitive to paxilline was not recorded in ciliary cells. Second, $DiBAC_4(3)$ cannot detect fast membrane potential changes. Third, the most serious limitation is that the exact membrane potential cannot be measured by $DiBAC_4(3)$, even though calibration under voltage-clamp is available (Yamada et al., 2001). The membrane hyperpolarization induced by 10 μM diazoxide appeared to be approximately 11 mV based on the calibration. This value was apparently larger than that directly recorded under current-clamp mode (4 mV). The reason for the dissociation between two measurements is not clear. It is, however, likely that the Cl^- conductance appears to be high compared with that of K^+ in ciliated cells. When the pipette filling solution contained 140 mM Cl^-, the resting membrane potential was extremely shallow (−19 mV) and close to equilibrium potential of Cl^- rather than K^+. Under these experimental conditions, the membrane hyperpolarization attributed to the K^+ conductance increase may be smaller than what occurs under normal Cl^- gradient across the cell membrane. The intracellular Cl^- concentration varied widely depending on cell types in a range of 5 and 30 mM but is unfortunately unknown in tracheal ciliated cells. Further study is required to understand the real membrane hyperpolarization by K_{ATP} channel opening in ciliary cells.

In this study, the membrane hyperpolarization increased the influx of Ca^{2+} presumably by an unknown pathway rather than by VDCC. The membrane hyperpolarization may simply increase the transmembrane driving force for Ca^{2+} through Ca^{2+} permeable channels with non–voltage-dependent gating mechanisms. Taken together, it can be suggested that K_{ATP} channel openers may have additional benefits, including an expectorant effect, for the therapy of occlusive respiratory disorders.

In conclusion, a K_{ATP} channel composed of Kir6.2/SUR2B and possibly also Kir6.1/SUR2B is functionally expressed in ciliated cells in mice airway epithelium. The activation of a K_{ATP} channel induces membrane hyperpolarization and results in an increase in Ca^{2+}-influx through a novel, non-VDCC pathway. The enhancement of the ciliary movement by K_{ATP} openers is mainly attributable to the Ca^{2+} rise and is considered to have an additional and beneficial effect on the

current drug therapies used to treat occlusive respiratory disorders.

Authorship Contributions

Participated in research design: Ohba, Sawada, Imaizumi.

Conducted experiments: Ohba, Sawada, Suzuki.

Performed data analysis: Ohba, Sawada, Yamamura, Ohya, Imaizumi.

Wrote or contributed to the writing of the manuscript: Tsuda, Imaizumi.

References

Braiman A, Gold'Shtein V, and Priel Z (2000) Feasibility of a sustained steep Ca^{2+} Gradient in the cytosol of electrically non-excitable cells. *J Theor Biol* **206**:115–130.

Braiman A and Priel Z (2001) Intracellular stores maintain stable cytosolic Ca^{2+} gradients in epithelial cells by active Ca^{2+} redistribution. *Cell Calcium* **30**:361–371.

Braiman A and Priel Z (2008) Efficient mucociliary transport relies on efficient regulation of ciliary beating. *Respir Physiol Neurobiol* **163**:202–207.

Chang LY, Wu R, and Nettesheim P (1985) Morphological changes in rat tracheal cells during the adaptive and early growth phase in primary cell culture. *J Cell Sci* **74**:283–301.

Clark R and Proks P (2010) ATP-sensitive potassium channels in health and disease. *Adv Exp Med Biol* **654**:165–192.

Dymek EE and Smith EF (2007) A conserved CaM- and radial spoke associated complex mediates regulation of flagellar dynein activity. *J Cell Biol* **179**:515–526.

Evans JH and Sanderson MJ (1999) Intracellular calcium oscillations regulate ciliary beat frequency of airway epithelial cells. *Cell Calcium* **26**:103–110.

Flagg TP, Enkvetchakul D, Koster JC, and Nichols CG (2010) Muscle K_{ATP} channels: recent insights to energy sensing and myoprotection. *Physiol Rev* **90**:799–829.

Fukuse T, Hirata T, Omasa M, and Wada H (2002) Effect of adenosine triphosphate-sensitive potassium channel openers on lung preservation. *Am J Respir Crit Care Med* **165**:1511–1515.

Funabashi K, Ohya S, Yamamura H, Hatano N, Muraki K, Giles W, and Imaizumi Y (2010) Accelerated Ca^{2+} entry by membrane hyperpolarization due to Ca^{2+}-activated K^+ channel activation in response to histamine in chondrocytes. *Am J Physiol Cell Physiol* **298**:C786–C797.

Garlid KD, Paucek P, Yarov-Yarovoy V, Sun X, and Schindler PA (1996) The mitochondrial K_{ATP} channel as a receptor for potassium channel openers. *J Biol Chem* **271**:8796–8799.

Grimmsmann T and Rustenbeck I (1998) Direct effects of diazoxide on mitochondria in pancreatic β-cells and on isolated liver mitochondria. *Br J Pharmacol* **123**: 781–788.

Hibino H, Inanobe A, Furutani K, Murakami S, Findlay I, and Kurachi Y (2010) Inwardly rectifying potassium channels: their structure, function, and physiological roles. *Physiol Rev* **90**:291–366.

Holmuhamedov EL, Wang L, and Terzic A (1999) ATP-sensitive K^+ channel openers prevent Ca^{2+} overload in rat cardiac mitochondria. *J Physiol* **519**:347–360.

Imaizumi Y, Muraki K, and Watanabe M (1989) Ionic currents in single smooth muscle cells from the ureter of the guinea-pig. *J Physiol* **411**:131–159.

Kawakami M, Nagira T, Hayashi T, Shimamoto C, Kubota T, Mori H, Yoshida H, and Nakahari T (2004) Hypo-osmotic potentiation of acetylcholine-stimulated ciliary beat frequency through ATP release in rat tracheal ciliary cells. *Exp Physiol* **89**:739–751.

Leroy C, Dagenais A, Berthiaume Y, and Brochiero E (2004) Molecular identity and function in transepithelial transport of K_{ATP} channels in alveolar epithelial cells. *Am J Physiol Lung Cell Mol Physiol* **286**:L1027–L1037.

Lorenzo IM, Liedtke W, Sanderson MJ, and Valverde MA (2008) TRPV4 channel participates in receptor-operated calcium entry and ciliary beat frequency regulation in mouse airway epithelial cells. *Proc Natl Acad Sci USA* **105**:12611–12616.

Ma W, Silberberg SD, and Priel Z (2002) Distinct axonemal processes underlie spontaneous and stimulated airway ciliary activity. *J Gen Physiol* **120**:875–885.

Malerba M, Radaeli A, Mancuso S, and Polosa R (2010) The potential therapeutic role of potassium channel modulators in asthma and chronic obstructive pulmonary disease. *J Biol Regul Homeost Agents* **24**:123–130.

Morimoto T, Sakamoto K, Sade H, Ohya S, Muraki K, and Imaizumi Y (2007) Voltage-sensitive oxonol dyes are novel large-conductance Ca^{2+}-activated K^+ channel activators selective for β1 and β4 but not for β2 subunits. *Mol Pharmacol* **71**:1075–1088.

O'Grady SM and Lee SY (2003) Chloride and potassium channel function in alveolar epithelial cells. *Am J Physiol Lung Cell Mol Physiol* **284**:L689–L700.

O'Rourke B (2004) Evidence for mitochondrial K^+ channels and their role in cardioprotection. *Circ Res* **94**:420–432.

Pelaia G, Gallelli L, Vatrella A, Grembiale RD, Maselli R, De Sarro GB, and Marsico SA (2002) Potential role of potassium channel openers in the treatment of asthma and chronic obstructive pulmonary disease. *Life Sci* **70**:977–990.

Rodrigo GC and Standen NB (2005) ATP-sensitive potassium channels. *Curr Pharm Des* **11**:1915–1940.

Sakato M, Sakakibara H, and King SM (2007) Chlamydomonas outer arm dynein alters conformation in response to Ca^{2+}. *Mol Biol Cell* **18**:3620–3634.

Salathe M (2007) Regulation of mammalian ciliary beating. *Annu Rev Physiol* **69**: 401–422.

Salathe M and Bookman RJ (1999) Mode of Ca^{2+} action on ciliary beat frequency in single ovine airway epithelial cells. *J Physiol* **520**:851–865.

Schmid A and Salathe M (2011) Ciliary beat co-ordination by calcium. *Biol Cell* **103**: 159–169.

Seybold ZV, Mariassy AT, Stroh D, Kim CS, Gazeroglu H, and Wanner A (1990) Mucociliary interaction in vitro: effects of physiological and inflammatory stimuli. *J Appl Physiol* **68**:1421–1426.

Shiima-Kinoshita C, Min KY, Hanafusa T, Mori H, and Nakahari T (2004) β2-adrenergic regulation of ciliary beat frequency in rat bronchiolar epithelium: potentiation by isosmotic cell shrinkage. *J Physiol* **554**:403–416.

Tarasiuk A, Bar-Shimon M, Gheber L, Korngreen A, Grossman Y, and Priel Z (1995) Extracellular ATP induces hyperpolarization and motility stimulation of ciliary cells. *Biophys J* **68**:1163–1169.

Trinh NT, Privé A, Kheir L, Bourret JC, Hijazi T, Amraei MG, Noël J, and Brochiero E (2007) Involvement of K_{ATP} and KvLQT1 K^+ channels in EGF-stimulated alveolar epithelial cell repair processes. *Am J Physiol Lung Cell Mol Physiol* **293**:L870–L882.

Trinh NT, Privé A, Maillé E, Noël J, and Brochiero E (2008) EGF and K^+ channel activity control normal and cystic fibrosis bronchial epithelia repair. *Am J Physiol Lung Cell Mol Physiol* **295**:L866–L880.

Weiss T, Gheber L, Shoshan-Barmatz V, and Priel Z (1992) Possible mechanism of ciliary stimulation by extracellular ATP: involvement of calcium-dependent potassium channels and exogenous Ca^{2+}. *J Membr Biol* **127**:185–193.

Woo SK, Kwon MS, Ivanov A, Gerzanich V, and Simard JM (2013) The sulfonylurea receptor 1 (Sur1)-transient receptor potential melastatin 4 (Trpm4) channel. *J Biol Chem* **288**:3655–3667.

Yamada A, Gaja N, Ohya S, Muraki K, Narita H, Ohwada T, and Imaizumi Y (2001) Usefulness and limitation of $DiBAC_4(3)$, a voltage-sensitive fluorescent dye, for the measurement of membrane potentials regulated by recombinant large conductance Ca^{2+}-activated K^+ channels in HEK293 cells. *Jpn J Pharmacol* **86**:342–350.

Yamada M and Kurachi Y (2005) A functional role of the C-terminal 42 amino acids of SUR2A and SUR2B in the physiology and pharmacology of cardiovascular ATP-sensitive K^+ channels. *J Mol Cell Cardiol* **39**:1–6.

Yamamura H, Ikeda C, Suzuki Y, Ohya S, and Imaizumi Y (2012) Molecular assembly and dynamics of fluorescent protein-tagged single $K_{Ca}1.1$ channel in expression system and vascular smooth muscle cells. *Am J Physiol Cell Physiol* **302**: C1257–C1268.

Yamazaki D, Kito H, Yamamoto S, Ohya S, Yamamura H, Asai K, and Imaizumi Y (2011) Contribution of K_v2 potassium channels to ATP-induced cell death in brain capillary endothelial cells and reconstructed HEK293 cell model. *Am J Physiol Cell Physiol* **300**:C75–C86.

Address correspondence to: Dr. Yuji Imaizumi, Department of Molecular and Cellular Pharmacology, Graduate School of Pharmaceutical Sciences, Nagoya City University, 3-1 Tanabedori, Mizuhoku, Nagoya 467-8603, Japan. E-mail: yimaizum@phar.nagoya-cu.ac.jp

J Toxicol Pathol 2013; 26: 335–341

Review

Colon Preneoplastic Lesions in Animal Models

Masumi Suzui[1*], Takamitsu Morioka[2], and Naoki Yoshimi[3]

[1] Department of Molecular Toxicology, Graduate School of Medical Sciences and Medical School, Nagoya City University, 1 Kawasumi, Mizuho-ku, Mizuho-cho, Nagoya 467-8601, Japan
[2] Radiation Effect Accumulation and Prevention Project, Fukushima Project Headquarters and Radiobiology for Children's Health Program, Research Center for Radiation Protection, National Institute of Radiological Sciences, 4-9-1 Anagawa, Inage-ku, Chiba 263-8555, Japan
[3] Department of Pathology and Oncology, Graduate School of Medicine and Faculty of Medicine, University of the Ryukyus Faculty of Medicine, 207 Uehara, Nishihara-cho, Okinawa 903-0215, Japan

Abstract: The animal model is a powerful and fundamental tool in the field of biochemical research including toxicology, carcinogenesis, cancer therapeutics and prevention. In the carcinogenesis animal model system, numerous examples of preneoplastic lesions have been isolated and investigated from various perspectives. This may indicate that several options of endpoints to evaluate carcinogenesis effect or therapeutic outcome are presently available; however, classification of preneoplastic lesions has become complicated. For instance, these lesions include aberrant crypt foci (ACF), dysplastic ACF, flat ACF, β-catenin accumulated crypts, and mucin-depleted foci. These lesions have been induced by commonly used chemical carcinogens such as azoxymethane (AOM), 1,2-dimethylhydrazine (DMH), methylnitrosourea (MUN), or 2-amino-1-methyl-6-phenylimidazo[4,5-*b*]pyridine (PhIP). Investigators can choose any procedures or methods to examine colonic preneoplastic lesions according to their interests and the objectives of their experiments. Based on topographical, histopathological, and biological features of colon cancer preneoplastic lesions in the animal model, we summarize and discuss the character and implications of these lesions. (DOI: 10.1293/tox.2013-0028; J Toxicol Pathol 2013; 26: 335–341)

Key words: preneoplastic lesion, colon carcinogenesis, animal model, topographic view

Aberrant Crypt Foci (ACF)

Bird[1] first reported in 1987 that when C57BL/6J mice were treated with azoxymethane (AOM), aberrant dysplastic crypts appeared in the colonic mucosa. After fixation with 10% buffered formalin and staining with methylene blue, these crypts were easily visualized in the topographic view of the colonic mucosa using a x4 objective (Fig. 1A). These lesions were referred to as aberrant crypts (AC) or aberrant crypt foci (ACF) in the colon of both animals and humans[2–4]. ACF were cryptic lesions distinguished by their increased size, thicker epithelial lining, and increased pericryptic zone[1]. ACF have only been seen in the colon of carcinogen-treated mice and rats. They have not been seen in the colon treated with a noncarcinogen or in untreated animals[2,3]. After carcinogen treatment, they appeared as early as within 2 weeks and persisted until the experimental termination of animals (16 weeks); histological changes from mild atypia to dysplasia[2] were also revealed. Two heterocyclic amines, 2-amino-3-methylimidazo[4,5-*f*]quinoline (IQ) and 2-amino-1-methyl-6-phenylimidazo[4,5-*b*]pyridine (PhIP), were shown to be able to induce ACF in the colon, respectively, after 4 and 10 weeks of exposure[5]. The number of ACF increased significantly over time, and small-sized ACF were predominant at all time points[5]. In histological slides, the large ACF exhibits dysplasia and thus can be termed a microadenoma[2].

ACF are also induced in the colonic mucosa of rats or mice treated with carcinogens such as AOM, methylazoxymethanol (MAM) acetate, 1,2-dimethylhydrazine (DMH), methylnitrosourea (MNU), PhIP, IQ, 2-amino-3,8-dimethylimidazo[4,5-*f*]quinoline (MeIQ) and 2-amino-6-methyldipyrido[1,2-*a*:3',2'-*d*]imidazole (Glu-P-1)[3,6–11]. In our previous experiments[7,12], F344 rats were subcutaneously (sc) injected with AOM (20 mg/kg body weight) twice. Five weeks after the beginning of the experiment, 93–139 ACF per colon occurred. When F344 rats were treated with AOM (15 mg/kg body weight, sc injection) 3 times, 240 ACF/colon occurred at 11 weeks after the beginning of the experiment[13]. When F344 rats were treated with DMH (40 mg/kg body weight, sc injection) twice, 175–200 ACF/colon were induced at 5 or 8 weeks after the beginning of the experiment[11,14,15]. These ACF usually contained 1–3 or more crypts per focus. The diameter of an aberrant crypt measured at least 3 to 4 times larger than that of a normal crypt

Received: 28 May 2013, Accepted: 27 June 2013
*Corresponding author: M Suzui (suzui@med.nagoya-cu.ac.jp)

in mice[2,16] and up to 1.5 times larger than a normal crypt in humans[17]. Pretlow *et al.*[16] reported that ACF were at least 3 times larger in diameter than normal crypts, and most ACF had lumina that were oval or slit shaped rather than circular. ACF range in size and have from 1 to 412 aberrant crypts per focus[17–20]. The size in the topographic view and the histologically dysplastic character of ACF are critical factors when we distinguish ACF as preneoplastic lesions. We consider that large ACF consisting of more than 10–20 crypts and manifesting dysplasia could be termed a microadenoma. In mouse models, for instance, B57BL/6J and CF_1 mice were given a single intraperitoneal (ip) injection of AOM (5 mg/kg body weight), and 4 weeks later, mice developed 2.6 and 3 ACF per colon, respectively[2]. BALB/c mice were ip injected with AOM (10 mg/kg body weight) twice, and 14 ACF were induced 4 weeks after the injection[21]. In C57BL/6J-*Min*/+ (*Min*) and C57BL/6J-+/+ (wild type) mice, PhIP was ip injected 4 times. Ten weeks after the injection, male mice developed 3 and 0 ACF, respectively, and female mice developed 1.9 and 0.2 ACF in their colons[22]. These findings indicate that duration of the experimental period, strain of animals, method of administration of carcinogens, and nature of carcinogen used as an initiator, may affect the number of ACF in the colonic mucosa.

In terms of the distribution of ACF, McLellan *et al.*[2] demonstrated that AOM-treated CF_1 mice developed ACF, 67% of which were in the rectal segment, 29% of which were in the middle segment and 4% of which were in the cecal segment. ACF were seen mainly in the rectal and middle segments when the animals were treated with DMH, NMU, MeIQ, or Glu-P-1[3]. Most ACF were found in the middle and distal colon in F344 rats treated with AOM[23]. In contrast, Hata *et al.*[24] demonstrated that ACF were frequently found in the proximal colon (cecal segment of the colon) when AKR/J and SWR/J mice were treated with AOM. The carcinogen IQ also induced ACF primarily in the middle and cecal segments of the colon[3]. Colon tumors induced by AOM were primarily found in distal colon rather than in proximal colon in the rat and mouse models[24,25], indicating that the correlation between ACF formation and carcinogenesis is not necessarily straightforward. This is presumably because of the heterogeneous nature of ACF[26–28]. Also, experimental protocol and species used may affect the difference in distribution of ACF[3,29–31].

The shape of the lumen of the ACF is relates to the histology of the ACF. Histological criteria of rat/mouse ACF have been described by several investigators[26,32]. Accordingly, ACF may be classified into the following 3 categories. In brief, these are (1) non dysplastic foci, which exhibit hyercellularity of uniform or normal looking goblet cells with basal-oriented nuclei and apical localization of mucus; (2) mild to moderate dysplastic foci, which exhibit hypercellularity of cells with elongated nuclei and focal nuclear stratification; and (3) moderate to severe dysplastic foci, which exhibit hypercellularity of elongated cells with abundant basophilic cytoplasm. These foci display enlarged and vesiculated nuclei, sometimes with prominent nucleoli.

Dysplastic ACF

The dysplastic nature of ACF was described by McLellan and Bird[2]. In a hematoxylin-eosin (HE) stained transverse section, ACF exhibited a focal appearance and mild cellular atypia, and dysplasia was observed in the large focus. Bird and Pretlow mentioned that use of the term dysplastic crypt foci to describe abnormal crypts is valid only if the investigators examined histologically all of the methylene blue-identified lesions and found dysplasia in all of them[33]. Ochiai *et al.*[34,35] described two distinct types of ACF in the PhIP-induced rat model. One was dysplastic ACF, and the other was nondysplastic ACF. In their reports, dysplastic ACF are histologically characterized by distortion of the crypt structure, a decrease in goblet cell number, existence of nuclear stratification, and enlarged nuclei. Nondysplastic ACF indicated the hyperplastic change in crypts. One-fourth of PhIP-induced ACF were dysplastic ACF, and the remaining ACF were nondysplastic ACF. Two-week dietary administration of 400 ppm PhIP was repeated three times with a 4-week interval. The average number of dysplastic ACF was up to 0.8 per colon, and they were larger in size than nondysplastic ACF after 32 weeks of experimentation. In the dysplastic ACF, cytoplasmic β-catenin protein accumulation and β-catenin gene mutation were found. The mutations were $^{32}A \rightarrow G$ (Asp→Gly), $^{34}G \rightarrow T$ (Gly→Val), and $^{36}C \rightarrow T$ (His→Tyr)[35]. By a staining method that uses 70% methanol followed by 0.2% methylene blue staining, dysplastic ACF can be topographically contrasted with nondysplastic ACF on the colonic mucosa and identified without performing histological examination[34]. The average number of dysplastic ACF/colon was 2.0–3.2 in F344 rats treated with PhIP (400 ppm in diet), MeIQ (300 ppm in diet), and IQ (300 ppm in diet). Two-week dietary administration of PhIP, MeIQ, or IQ was repeated three times with a 4-week interval. Other investigators[26,32,34,36] have also described dysplastic ACF. Thorup[32] found that a correlation between degree of dysplasia and crypt multiplicity, indicating that chemically induced ACF can increase in crypt multiplicity over time and progress into a tumor and that hyperplastic human ACF can also develop into adenomatous ACF, as reported elsewhere[37,38]. However, this view disagrees with that of other studies[39–41] demonstrating that the degree of dysplasia is not necessarily related to the crypt multiplicity.

Flat ACF

Paulsen *et al.*[42] examined unsectioned methylene blue-stained colon tissues obtained from male F344 rats treated with AOM (sc injection ×2 times, 15 mg/kg body weight), and found two types of early lesions. One was classic elevated ACF, and the other was flat ACF. Classical ACF were seen as enlarged crypts that were elevated from the surrounding epithelium and had elongated luminal openings. However, Paulsen *et al.*[42] described flat ACF as structures that were not elevated. The bright blue appearance and compressed pit pattern of flat ACF were used as criteria for identification.

Flat ACF were characterized by enlarged or small crypts that were not elevated from the epithelium and had round or elongated luminal openings. The investigators also described histological findings of flat ACF with severe dysplasia. In immunohistochemical analysis, classic elevated ACF did not show (0 of 99) cytoplasmic/nuclear expression of the β-catenin protein. In contrast, all flat ACF (8 of 8) displayed cytoplasmic/nuclear expression of the β-catenin protein. The number of classic elevated ACF decreased along with time. Their crypt multiplicity increased during the time period. The number of flat ACF decreased along time, and that of tumors increased correspondingly. The numbers of flat ACF plus tumors were virtually constant. In view of these findings, Paulsen *et al.*[42] concluded that flat ACF display a continuous development from early stages into a tumor.

β-Catenin Accumulated Crypts (BCAC)

In a previous study, we[43] found that focal lesions that display accumulation of the β-catenin protein predispose to carcinogen-induced colon carcinogenesis. We named these lesions β-catenin-accumulated crypts (BCAC) (Fig. 1B). F344 rats were treated with AOM (sc injection ×3 times, 15 mg/kg body weight), and a complete autopsy was performed at 10 weeks after the first AOM treatment[43]. In the topographical view in which colon tissues were stained with methylene blue, we found distinct populations of altered crypts named histologically altered crypts with macroscopically normal-like appearance (HACN) among the tissue samples. In HACN, which are equivalent to BCAC, the *β-catenin* gene was frequently mutated in 10 of 15 samples (67%), and the cytoplasmic β-catenin protein was accumulated in 13 of 15 samples (86%)[43]. Among these lesions, there were ^{28}A→T (Gln→His), ^{29}C→G (Ser→Cys), ^{30}T→C (Tyr→His), ^{32}G→A (Asp→Asn), ^{34}G→A (Gky→Glu), ^{34}G→T (Gly→stop), and ^{41}A→T (Thr→Ile) mutations. Because the lesion in which the β-catenin protein accumulated was considered to be valid in AOM-treated rat colonic mucosa, a time course study was done to examine the status of the protein accumulation, the number of crypts/lesion, and the diameter of the crypts[44]. Both the number of crypts/lesion and the diameter of the β-catenin accumulated crypts that were identified with immunohistochemical analysis significantly increased with the time course[24]. The number of BCAC induced by AOM in AKR/J and SWR/J mice varied by 3–12 per cm^2, and multiplicity was about 3–4 in both strains[24]. Histological abnormality of the crypts and cell proliferation also significantly increased when compared with those of ACF, indicating that BCAC are preneoplastic lesions in AOM-induced colon carcinogenesis[44].

Mucin-depleted Foci (MDF)

Caderni *et al.*[45] identified specific lesions in the colon of rats treated with AOM. When unsectioned colon tissues were stained with high-iron diamine-Alcian blue (HID-AB), foci of crypts with scarce or absent mucins were seen, and such lesions were first defined as mucin-depleted foci (MDF) (Fig. 1C). In that study, male F344 rats received sc injection of AOM (15 mg/kg body weight) twice. The rats developed approximately 4 and 8 MDF/colon at 7 and 15 weeks, respectively, after the start of the experiment, while 271–289 ACF/colon occurred during the same period. Mutations in *β-catenin*, *Apc*, and *K-ras* genes and cytoplasmic β-catenin expression were found in MDF induced by DMH[46–48]. Among these, *β-catenin* gene mutations included ^{32}G→A (Asp→Asn), ^{37}C→T (Ser→Phe), ^{33}C→T (Ser→Phe), and ^{41}C→T (Thr→Ile). In DMH studies, MDF exhibit dysplastic features, and the induction rate of MDF is dose dependent[45,47]. Also, MDF increase in size with time. To examine the multiplicity and distribution of ACF, MDF, and tumors, six-week-old F344 rats were treated with DMH (40 mg/kg body weight sc injection twice a week) followed by 1% dextran sodium sulfate in drinking water. At ten and fourteen weeks after the start of the experiment, animals were euthanized. ACF were mainly found in the middle portion of the colon (Fig. 2A). MDF and tumors occurred more in the distal portion than in the proximal portion (Fig. 2B and C). These results were in accordance with those in the report of Femia *et al*[47]. They found that DMH-induced MDF and tumors were mainly found in the distal portion of the colon, while "classical" ACF were found more predominantly in the middle portion of the colon[47]. Also, Femia *et al.* mentioned that with regard to the ability of ACF/MDF as a biomarker predicting the carcinogenesis status, the heterogeneous nature of each lesion may be related[49].

Only a limited number of findings on MDF are currently available; based on those that are available, Femia and Caderny[27] conclude that MDF are premalignant lesions for colon carcinogenesis and a promising biomarker for study of the effect of chemopreventive agents in colon carcinogenesis. MDF may provide a reliable option as biomarkers for colon carcinogenesis, and it is thought that production or deletion of mucin or both plays some roles in the development of colon tumors. To reiterate, MDF may have both morphological and biochemical aspects as a biomarker. To identify MDF, we[11] demonstrated a simple staining method using 1% Alcian blue (pH 2.5) solution instead of the original HID-AB staining method. In this study, male F344 received sc injections of DMH (40 mg/kg body weight) twice, and the rats developed 19 MDF/colon and 150 ACF/colon at 8 weeks after the start of the experiment. By comparing exact locations of MDF and BCAC on the face-up mucosal samples and by conducting Alcian blue/HE/immunohistochemical staining, we[11] found that MDF are practically identical to BCAC and useful as an early biomarker in rat colon carcinogenesis. In human specimens obtained from patients with colorectal carcinoma (CRC) and familial adenomatous polyposis (FAP), MDF were also identified[50]. The mean numbers of crypts/MDF were 60 and 33 in samples of patients with CRC and FAP, respectively. In a CRC case, the histological diagnosis of MDF was microadenoma with moderate grade dysplasia, while in cases of FAP, the diagnosis was microadenoma with low-grade dysplasia[50]. In a recent

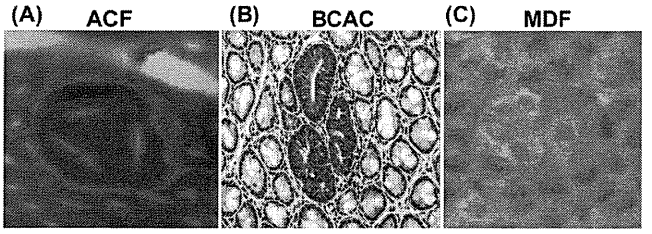

Fig. 1. Topographic views of (A) ACF, (B) BCAC, and (C) MDF. (A) Note that three identical crypts are seen in one focus (methylene blue staining). (B) Crypts with accumulations of β-catenin protein in cytoplasm are present (immunohistochemical staining). (C) A focal lesion characterized by the absence or very small production of mucin (seen as very thin blue-stained crypts) is present (high-iron diamine-Alcian blue staining). ACF, aberrant crypt foci; BCAC, β-catenin accumulated crypts; MDF, mucin-depleted foci.

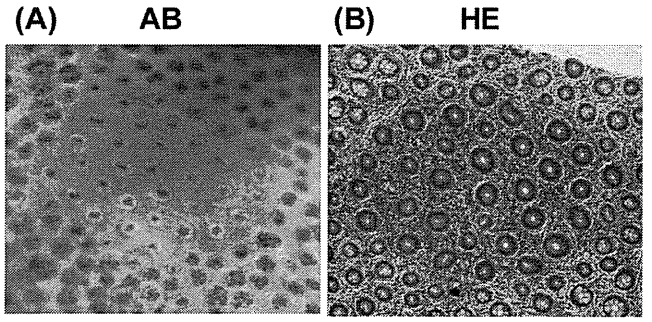

Fig. 3. Topographic views of human MDF stained with (A) 1% Alcian blue (pH 2.5) and (B) hematoxylin and eosin. MDF were identified as focal lesions characterized by loss of Alcian blue staining, attributable to the loss of mucin, as compared with the surrounding normal crypts. AB, Alcian blue; HE, hematoxylin and eosin.

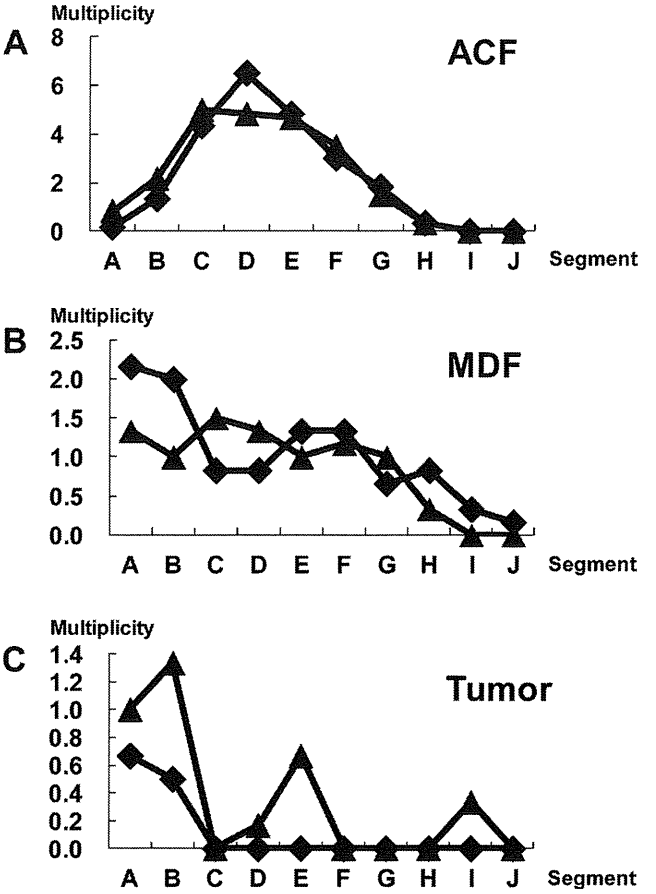

Fig. 2. Distribution of ACF, MDF, and tumors in each segment (A-J) along the colon. The x-axis indicates the segments from the distal to proximal colon. Each segment was named A to J in 2-cm intervals from the anal side. The y-axis indicates the average number of lesions per colon (multiplicity). At ten (closed diamond) and fourteen weeks (closed triangle) after the start of the experiment, animals were euthanized. After fixing of colon tissues with 10% buffered formalin on a filter paper with the mucosal surface up, colon tissues were stained with a 1% solution of Alcian blue, pH 2.5, in 3% acetic acid for 5 min and immediately washed with distilled water. Subsequently, after detection of MDF, the colon tissue was stained with 0.2% methylene blue solution to identify ACF. ACF, MDF, and tumors were noted grossly for their location, number, and size as described earlier[11]. The animal experiment was conducted according to the Institutional Animal Care Guidelines.

study, our group[51] examined human CRC cases and found MDF on the colonic mucosa. The lesion was histologically classified into two categories: flat MDF and protruded MDF. The former lesion did not show nuclear stratification or loss of polarity, but showed Paneth cell metaplasia and decrease/loss of goblet cells, indicative of low-grade dysplasia. Protruded MDF displayed the features of both ACF and MDF, also corresponding to low-grade dysplasia. A topographic view of human MDF is shown in Fig. 3.

Conclusions

This review summarizes topographical, histopathological, and biological features of preneoplastic lesions that have been described in colon carcinogenesis models of the rodent (Table 1). The early lesion has been identified and documented as a preneoplastic lesion in the carcinogenesis process. However, the fact that even the verified lesions appear to contain neoplastic lesions such as a microadenoma indicates the need for further investigation. This may be due to complicated categories or classifications of preneoplastic lesions. Considering the 3R principles (which commonly consist of replacement of methods with no animal use, reduction of the number of test animals, and refinement of methods that minimize the suffering of test animals), a short-term experiment in which an early preneoplastic lesion occurs and can be used as a biomarker should be used to examine toxicity and/or carcinogenicity of test compounds in a specific organ site. In this context, investigators can choose any procedures or methods to examine colonic preneoplastic lesions according to their interests and the objectives of their experiments.

Table 1. Summary of Characters of Preneoplastic Lesions in the Animal Model

Practical name of the lesion	Ref. no. of the current article	Staining method	Features in topographic and/or histological views	
ACF	1, 2, 11, 26, 32	Methelene blue staining	In topographic view, increased cryptial size, thicker epilbelial linig, and increased pericryptical zone.	
		Hematoxylin-eosin (HE) staining	Histological criteria of ACF	
			(1) Non dysplastic foci	Hyercellularity of uniform or normal looking goblet cells with basal-oriented nuclei and apical localization of mucus.
			(2) Mild to moderate dysplastic foci	Hypercellularity of cells with elongated nuclei and focal nuclear stratification.
			(3) Moderate to severe dysplastic foci	Hypercellularity of elongated cells with abundant basophilic cytoplasm. These foci display enlarged and vesiculated nuclei, sometimes with prominent nucleoli.
			Subtype: dysplastic foci	Focal lesions with nuclear stratification, loss of nuclear polarity, structural abnormality of the crypts, Paneth cell metaplasia, a decrease or loss of goblet cells, and presence of mitosis.
Dysplastic ACF	26, 32, 34–36	HE staining	Histologically characterized by distortion of the crypt structure, a decrease in goblet cell number, nuclear stratification, and enlarged nuclei.	
Flat ACF	42	Methelene blue staining	Characterized by bright blue staining, enlarged or small crypts not elevated from the epithelium and round or elongated luminal openings. Because the flat ACF were not observed as elevated structures, their bright blue appearance and compressed pit pattern were used for identification.	
BCAC	24, 43, 44	Immuno-histochemical staining	Accumulation of cytoplasmic β-catenin protein. Crypts of BCAC do not display prominent epithelial cells in a topographic view.	
MDF	11, 45–50	High-iron diamine Alcian blue (HID-AB) staining 1% AB, pH2.5	When colon tissues were stained with HID-AB, foci of crypts with scarce or absent mucin were defined as MDF. MDF can be stained with 1% AB solution.	

ACF, aberrant crypt foci; BCAC, β-catenin accumulated crypts; MDF, mucin-depleted foci.

Acknowledgment: We thank Dr. Tatsuya Kinjo (Department of Digestive and General Surgery, University of the Ryukyus Graduate School of Medicine and Faculty of Medicine, Okinawa, Japan) for valuable comments and discussions. This work was supported in part by a Grant-in-Aid from the Ministry of Education, Culture, Sports, Science and Technology of Japan and a Grant-in-Aid from the Ministry of Health, Labour and Welfare.

References

1. Bird RP. Observation and quantification of aberrant crypts in the murine colon treated with a colon carcinogen: preliminary findings. Cancer Lett. **37**: 147–151. 1987. [Medline]
2. McLellan EA, and Bird RP. Aberrant crypts: potential preneoplastic lesions in the murine colon. Cancer Res. **48**: 6187–6192. 1988. [Medline]
3. Tudek B, Bird RP, and Bruce WR. Foci of aberrant crypts in the colons of mice and rats exposed to carcinogens associated with foods. Cancer Res. **49**: 1236–1240. 1989. [Medline]
4. Roncucci L, Stamp D, Medline A, Cullen JB, and Bruce WR. Identification and quantification of aberrant crypt foci and microadenomas in the human colon. Hum Pathol. **22**: 287–294. 1991. [Medline]
5. Kristiansen E. The role of aberrant crypt foci induced by the two heterocyclic amines 2-amino-3-methyl-imidazo[4,5-*f*]quinoline (IQ) and 2-amino-1-methyl-6-phenylimidazo[4,5-*b*]pyridine (PhIP) in the development of colon cancer in mice. Cancer Lett. **110**: 187–192. 1996. [Medline]
6. Bird RP. Role of aberrant crypt foci in understanding the pathogenesis of colon cancer. Cancer Lett. **93**: 55–71. 1995. [Medline]
7. Morioka T, Suzui M, Nabandith V, Inamine M, Aniya Y, Nakayama T, Ichiba T, Mori H, and Yoshimi N. The modifying effect of *Peucedanum japonicum*, a herb in the Ryukyu Islands, on azoxymethane-induced colon preneoplastic lesions in male F344 rats. Cancer Lett. **205**: 133–141. 2004. [Medline]
8. Mori Y, Yoshimi N, Iwata H, Tanaka T, and Mori H. The synergistic effect of 1-hydroxyanthraquinone on methylazoxymethanol acetate-induced carcinogenesis in rats. Carcinogenesis. **12**: 335–338. 1991. [Medline]
9. Chewonarin T, Kinouchi T, Kataoka K, Arimochi H, Kuwahara T, Vinitketkumnuen U, and Ohnishi Y. Effects of roselle (Hibiscus sabdariffa Linn.), a Thai medicinal plant, on the mutagenicity of various known mutagens in Salmonella typhimurium and on formation of aberrant crypt foci induced by the colon carcinogens azoxymethane and 2-amino-1-methyl-6-phenylimidazo[4,5-*b*]pyridine in F344 rats. Food Chem Toxicol. **37**: 591–601. 1999. [Medline]
10. Sohn OS, Fiala ES, Requeijo SP, Weisburger JH, and Gonzalez FJ. Differential effects of CYP2E1 status on the meta-

bolic activation of the colon carcinogens azoxymethane and methylazoxymethanol. Cancer Res. **61**: 8435–8440. 2001. [Medline]

11. Yoshimi N, Morioka T, Kinjo T, Inamine M, Kaneshiro T, Shimizu T, Suzui M, Yamada Y, and Mori H. Histological and immunohistochemical observations of mucin-depleted foci (MDF) stained with Alcian blue, in rat colon carcinogenesis induced with 1,2-dimethylhydrazine dihydrochloride. Cancer Sci. **95**: 792–797. 2004. [Medline]
12. Morioka T, Suzui M, Nabandith V, Inamine M, Aniya Y, Nakayama T, Chiba T, and Yoshimi N. Modifying effects of Terminalia catappa on azoxymethane-induced colon carcinogenesis in male F344 rats. Eur J Cancer Prev. **14**: 101–105. 2005. [Medline]
13. Asano N, Kuno T, Hirose Y, Yamada Y, Yoshida K, Tomita H, Nakamura Y, and Mori H. Preventive effects of a flavonoid myricitrin on the formation of azoxymethane-induced premalignant lesions in colons of rats. Asian Pac J Cancer Prev. **8**: 73–76. 2007. [Medline]
14. Nabandith V, Suzui M, Morioka T, Kaneshiro T, Kinjo T, Matsumoto K, Akao Y, Iinuma M, and Yoshimi N. Inhibitory effects of crude α-mangostin, a xanthone derivative, on two different categories of colon preneoplastic lesions induced by 1, 2-dimethylhydrazine in the rat. Asian Pac J Cancer Prev. **5**: 433–438. 2004. [Medline]
15. Inamine M, Suzui M, Morioka T, Kinjo T, Kaneshiro T, Sugishita T, Okada T, and Yoshimi N. Inhibitory effect of dietary monoglucosylceramide 1-O-β-glucosyl-*N*-2'-hydroxyarachidoyl-4,8-sphingadienine on two different categories of colon preneoplastic lesions induced by 1,2-dimethylhydrazine in F344 rats. Cancer Sci. **96**: 876–881. 2005. [Medline]
16. Pretlow TP, Barrow BJ, Ashton WS, O'Riordan MA, Pretlow TG, Jurcisek JA, and Stellato TA. Aberrant crypts: putative preneoplastic foci in human colonic mucosa. Cancer Res. **51**: 1564–1567. 1991. [Medline]
17. Fenoglio-Preiser CM, and Noffsinger A. Aberrant crypt foci: A review. Toxicol Pathol. **27**: 632–642. 1999. [Medline]
18. Di Gregorio C, Losi L, Fante R, Modica S, Ghidoni M, Pedroni M, Tamassia MG, Gafà L, Ponz de Leon M, and Roncucci L. Histology of aberrant crypt foci in the human colon. Histopathology. **30**: 328–334. 1997. [Medline]
19. Nucci MR, Robinson CR, Longo P, Campbell P, and Hamilton SR. Phenotypic and genotypic characteristics of aberrant crypt foci in human colorectal mucosa. Hum Pathol. **28**: 1396–1407. 1997. [Medline]
20. Shpitz B, Bomstein Y, Mekori Y, Cohen R, Kaufman Z, Neufeld D, Galkin M, and Bernheim J. Aberrant crypt foci in human colons: distribution and histomorphologic characteristics. Hum Pathol. **29**: 469–475. 1998. [Medline]
21. Osawa E, Nakajima A, and Wada K, ishimine S, Fujisawa N, Kawamori T, Matsuhashi N, Kadowaki T, Ochiai M, Sekihara H, and Nakagama H. Peroxisome proliferator-activated receptor gamma ligands suppress colon carcinogenesis induced by azoxymethane in mice. Gastroenterology. **124**: 361–367. 2003. [Medline]
22. Steffensen IL, Paulsen JE, Eide TJ, and Alexander J. 2-Amino-1-methyl-6-phenylimidazo[4,5-*b*]pyridine increases the numbers of tumors, cystic crypts and aberrant crypt foci in multiple intestinal neoplasia mice. Carcinogenesis. **18**: 1049–1054. 1997. [Medline]
23. Shih CK, Chiang W, and Kuo ML. Effects of adlay on azoxymethane-induced colon carcinogenesis in rats. Food Chem Toxicol. **42**: 1339–1347. 2004. [Medline]
24. Hata K, Yamada Y, Kuno T, Hirose Y, Hara A, Qiang SH, and Mori H. Tumor formation is correlated with expression of β-catenin-accumulated crypts in azoxymethane-induced colon carcinogenesis in mice. Cancer Sci. **95**: 316–320. 2004. [Medline]
25. Holt PR, Mokuolu AO, Distler P, Liu T, and Reddy BS. Regional distribution of carcinogen-induced colonic neoplasia in the rat. Nutr Cancer. **25**: 129–135. 1996. [Medline]
26. Papanikolaou A, Wang QS, Papanikolaou D, Whiteley HE, and Rosenberg DW. Sequential and morphological analyses of aberrant crypt foci formation in mice of differing susceptibility to azoxymethane-induced colon carcinogenesis. Carcinogenesis. **21**: 1567–1572. 2000. [Medline]
27. Femia AP, and Caderni G. Rodent models of colon carcinogenesis for the study of chemopreventive activity of natural products. Planta Med. **74**: 1602–1607. 2008. [Medline]
28. Lance P, and Hamilton SR. Sporadic aberrant crypt foci are not a surrogate endpoint for colorectal adenoma prevention. Cancer Prev Res (Phila). **1**: 4–8. 2008. [Medline]
29. Carter JW, Lancaster HK, Hardman WE, and Cameron IL. Distribution of intestine-associated lymphoid tissue, aberrant crypt foci, and tumors in the large bowel of 1,2-dimethylhydrazine-treated mice. Cancer Res. **54**: 4304–4307. 1994. [Medline]
30. Maskens AP. Histogenesis and growth pattern of 1,2-dimethylhydrazine-induced rat colon adenocarcinoma. Cancer Res. **36**: 1585–1592. 1976. [Medline]
31. Glauert HP, and Weeks JA. Dose- and time-response of colon carcinogenesis in Fischer-344 rats after a single dose of 1,2-dimethylhydrazine. Toxicol Lett. **48**: 283–287. 1989. [Medline]
32. Thorup I. Histomorphological and immunohistochemical characterization of colonic aberrant crypt foci in rats: relationship to growth factor expression. Carcinogenesis. **18**: 465–472. 1997. [Medline]
33. Bird RP, and Pretlow TP. Correspondence re: Giovanna C et al., Effect of dietary carbohydrates on the growth of dysplastic crypt foci in the colon of rats treated with 1,2-dimethylhydrazine. Cancer Res., 51: 3721-3725, 1991. Cancer Res. **52**: 4291–4292. 1992. [Medline]
34. Ochiai M, Watanabe M, Nakanishi M, Taguchi A, Sugimura T, and Nakagama H. Differential staining of dysplastic aberrant crypt foci in the colon facilitates prediction of carcinogenic potentials of chemicals in rats. Cancer Lett. **220**: 67–74. 2005. [Medline]
35. Ochiai M, Ushigome M, Fujiwara K, Ubagai T, Kawamori T, Sugimura T, Nagao M, and Nakagama H. Characterization of dysplastic aberrant crypt foci in the rat colon induced by 2-amino-1-methyl-6-phenylimidazo[4,5-*b*]pyridine. Am J Pathol. **163**: 1607–1614. 2003. [Medline]
36. Paulsen JE, Steffensen IL, Loberg EM, Husoy T, Namork E, and Alexander J. Qualitative and quantitative relationship between dysplastic aberrant crypt foci and tumorigenesis in the Min/+ mouse colon. Cancer Res. **61**: 5010–5015. 2001. [Medline]
37. Kristiansen E, Thorup I, and Meyer O. Influence of different diets on development of DMH-induced aberrant crypt foci and colon tumor incidence in Wistar rats. Nutr Cancer. **23**: 151–159. 1995. [Medline]

38. Otori K, Sugiyama K, Hasebe T, Fukushima S, and Esumi H. Emergence of adenomatous aberrant crypt foci (ACF) from hyperplastic ACF with concomitant increase in cell proliferation. Cancer Res. **55**: 4743–4746. 1995. [Medline]
39. McLellan EA, Medline A, and Bird RP. Sequential analyses of the growth and morphological characteristics of aberrant crypt foci: putative preneoplastic lesions. Cancer Res. **51**: 5270–5274. 1991. [Medline]
40. Yamashita N, Minamoto T, Ochiai A, Onda M, and Esumi H. Frequent and characteristic K-ras activation in aberrant crypt foci of colon. Is there preference among K-ras mutants for malignant progression? Cancer. **75**: 1527–1533. 1995. [Medline]
41. Pretlow TP, Roukhadze EV, O'Riordan MA, Chan JC, Amini SB, and Stellato TA. Carcinoembryonic antigen in human colonic aberrant crypt foci. Gastroenterology. **107**: 1719–1725. 1994. [Medline]
42. Paulsen JE, Loberg EM, Olstorn HB, Knutsen H, Steffensen IL, and Alexander J. Flat dysplastic aberrant crypt foci are related to tumorigenesis in the colon of azoxymethane-treated rat. Cancer Res. **65**: 121–129. 2005. [Medline]
43. Yamada Y, Yoshimi N, Hirose Y, Kawabata K, Matsunaga K, Shimizu M, Hara A, and Mori H. Frequent *β-catenin* gene mutations and accumulations of the protein in the putative preneoplastic lesions lacking macroscopic aberrant crypt foci appearance, in rat colon carcinogenesis. Cancer Res. **60**: 3323–3327. 2000. [Medline]
44. Yamada Y, Yoshimi N, Hirose Y, Matsunaga K, Katayama M, Sakata K, Shimizu M, Kuno T, and Mori H. Sequential analysis of morphological and biological properties of β-catenin-accumulated crypts, provable premalignant lesions independent of aberrant crypt foci in rat colon carcinogenesis. Cancer Res. **61**: 1874–1878. 2001. [Medline]
45. Caderni G, Femia AP, Giannini A, Favuzza A, Luceri C, Salvadori M, and Dolara P. Identification of mucin-depleted foci in the unsectioned colon of azoxymethane-treated rats: correlation with carcinogenesis. Cancer Res. **63**: 2388–2392. 2003. [Medline]
46. Femia AP, Dolara P, Giannini A, Salvadori M, Biggeri A, and Caderni G. Frequent mutation of Apc gene in rat colon tumors and mucin-depleted foci, preneoplastic lesions in experimental colon carcinogenesis. Cancer Res. **67**: 445–449. 2007. [Medline]
47. Femia AP, Bendinelli B, Giannini A, Salvadori M, Pinzani P, Dolara P, and Caderni G. Mucin-depleted foci have beta-catenin gene mutations, altered expression of its protein, and are dose- and time-dependent in the colon of 1,2-dimethylhydrazine-treated rats. Int J Cancer. **116**: 9–15. 2005. [Medline]
48. Femia AP, Tarquini E, Salvadori M, Ferri S, Giannini A, Dolara P, and Caderni G. K-ras mutations and mucin profile in preneoplastic lesions and colon tumors induced in rats by 1,2-dimethylhydrazine. Int J Cancer. **122**: 117–123. 2008. [Medline]
49. Femia AP, Dolara P, and Caderni G. Mucin-depleted foci (MDF) in the colon of rats treated with azoxymethane (AOM) are useful biomarkers for colon carcinogenesis. Carcinogenesis. **25**: 277–281. 2004. [Medline]
50. Femia AP, Giannini A, Fazi M, and Tarquini E. salvadori M, Roncucci L, Tonelli F, and Dolara P, Caderni G. Identification of mucin depleted foci in the human colon. Cancer Prev Res (Phila). **1**: 562–567. 2008. [Medline]
51. Sakai E, Morioka T, Yamada E, Ohkubo H, Higurashi T, Hosono K, Endo H, Takahashi H, Takamatsu R, Cui C, Shinozawa M, Araike M, Samura H, Nishimaki T, Nakajima A, and Yoshimi N. Identification of preneoplastic lesions as mucin-depleted foci in patients with sporadic colorectal cancer. Cancer Sci. **103**: 144–149. 2012. [Medline]

Promotive effects of cell proliferation and chromosomal instability induced by tribbles-related protein 3 in mouse mammary tumor cells

YUTO SAKAI[1,2], KATSUMI FUKAMACHI[1], MITSURU FUTAKUCHI[1], HIDETOSHI HAYASHI[2] and MASUMI SUZUI[1]

[1]Department of Molecular Toxicology, Nagoya City University Graduate School of Medical Sciences and Medical School, 1 Kawasumi, Mizuho-cho, Mizuho-ku, Nagoya 467-8601; [2]Department of Drug Metabolism and Disposition, Nagoya City University Graduate School of Pharmaceutical Sciences, 3-1 Tanabe-dori, Mizuho-ku, Nagoya 467-8603, Japan

Received January 23, 2013; Accepted March 28, 2013

DOI: 10.3892/or.2013.2441

Abstract. Tribbles-related protein 3 (TRB3) has been shown to be a crucial modulator of tumorigenesis. However, the precise role and the functional morphology of TRB3 are not clearly understood. To elucidate these enigmas we established the cell line, M2TRB3, by introducing the human TRB3 gene and protein in Cl66M2 (M2) mouse mammary tumor cells. This cell line stably expressed the TRB3 gene and protein. After 72 h of cell culture, there was a 34% increase in the growth of M2TRB3 cells compared to the control M2 mock cells. The mean volume of the tumors originating from the M2TRB3 cells was significantly increased by 38% when compared to the mean volume of the M2 mock tumors, and the proliferating cell nuclear antigen (PCNA) labeling index in the M2TRB3 tumors was higher when compared to that of the M2 and M2 mock cells. In the tumor tissue samples, the mean diameter of nuclei in the M2TRB3 tumor cells (9.4±0.3 μm) showed a significant increase compared to that of the M2 mock tumor cells (7.0±0.2 μm). M2TRB3 cells also showed a marked increase in the population of tetraploid or octaploid nuclei compared to M2 mock cells bearing mainly either diploid or tetraploid nuclei. Western blot analysis revealed the overexpression of cyclin B1 and cyclin D1 in M2TRB3 cells when compared to that in the M2 mock cells. These novel findings provide further evidence that TRB3 promotes cell proliferation and chromosomal instability by causing polyploidization during development.

Correspondence to: Dr Masumi Suzui, Department of Molecular Toxicology, Nagoya City University Graduate School of Medical Sciences and Medical School, 1 Kawasumi, Mizuho-cho, Mizuho-ku, Nagoya 467-8601, Japan
E-mail: suzui@med.nagoya-cu.ac.jp

Key words: tribbles-related protein 3, cell proliferation, ploidy, tumor xenograft

Introduction

Tribbles-related protein 3 (TRB3, also known as NIPK, SKIP3) is a mammalian homologue of the *Drosophila Tribbles* gene, and this gene has been identified as an inhibitor of mitosis that regulates cell proliferation, migration and morphogenesis during development (1-3). Among tribbles homologues TRB1, TRB2 and TRB3, TRB3 is the most recently defined family of pseudokinases that contain a serine/threonine kinase catalytic domain but lack an ATP binding site or one of the conserved catalytic motifs essential for kinase activity (4). The interacting partners of TRB3 range from transcription factors, ubiquitin ligase, bone morphogenetic protein (BMP) type II receptor to members of the mitogen-activated protein kinase (MAPK) and phosphoinositide 3-kinase (PI3K) signaling pathways. By interacting with these proteins, it coordinates crucial cellular processes, including glucose/lipid metabolism, apoptosis, adipocyte differentiation, cell stress and regulation of collagen expression (5-9). We previously demonstrated that TRB3 is induced by C/EBP homologous protein (CHOP) and activating transcription factor 4 (ATF4) to regulate their function and endoplasmic reticulum (ER) stress-induced cell death (10) and that TRB3 also regulates the stability of cell division cycle 25A (Cdc25A), an essential activator of cyclin-dependent kinases (CDKs) (11).

Recent studies indicate that the three mammalian tribbles homologues are crucial modulators of tumorigenesis. For instance, both TRB1 and TRB2 are involved in myeloid leukemogenesis (12,13). TRB3 is highly expressed in a wide range of human carcinoma cell lines and in several types of human carcinomas (4,14). However, a precise role of TRB3 in tumorigenesis remains unknown. The aim of the present study was to examine whether the introduction of the human *TRB3* gene into mouse mammary tumor cells affects *in vitro*/*in vivo* growth and chromosomal stability during cell division of tumor cells.

Materials and methods

Cell culture. The human embryonic kidney cell line 293 purchased from the American Type Culture Collection (ATCC,

Manassas, VA, USA) and the human hepatocellular carcinoma cell line HepG2 were cultured in Dulbecco's modified Eagle's medium (DMEM; Wako Pure Chemical Industries, Ltd., Osaka, Japan) supplemented with 10% fetal bovine serum (FBS; Life Technologies, Inc., Rockville, MD, USA) in a humidified incubator with 5% CO_2 at 37˚C. The murine mammary tumor cell line Cl66M2 (M2) was generously provided by Dr Rakesh K. Singh (University of Nebraska Medical Center, Omaha, NE, USA) (18) and cultured in DMEM supplemented with 5% FBS in a humidified incubator with 5% CO_2 at 37˚C.

Construction of the expression vector. The TRB3 flag-tagged expression vector was constructed by ligating the full length human TRB3 cDNA into *Bam*HI and *Xho*I restriction sites of pcDNA3.1-Hygro (Life Technologies, Inc.) (9). The construct was verified by sequencing.

Preparation of a cell line that stably expresses the TRB3 gene. The expression vector pcDNA3.1-Hygro-flag-human TRB3 was transfected into Cl66M2 cells using Lipofectamine 2000 reagent (Life Technologies, Inc.). This cell line was termed M2TRB3. After transfection, the clone of the cells stably expressing M2TRB3 was selected by a limiting-dilution method in culture media supplemented with hygromycin. The cells transfected with the empty vector were also prepared as the control (M2mock). In M2TRB3 and M2mock cells, the levels of mRNA and protein expression were confirmed by reverse transcription-polymerase chain reaction (RT-PCR) and western blot assays.

In vitro cell proliferation assay. These assays were performed as described previously by us (15). Two murine mammary tumor cell lines M2TRB3 and M2mock were plated into 6-well 35-mm diameter culture plates ($1.0x10^4$ cells/well) in DMEM containing 10% FBS. Cells were starved in DMEM containing 0.5% FBS for 48 h. After starvation, the culture media were removed and cells were grown in DMEM containing 10% FBS for the indicated time course (0-72 h). The cells were washed twice with phosphate-buffered saline (PBS), harvested, resuspended in 1 ml PBS and the number of cells was determined using a hemocytometer Burker-Turk (Erma Inc., Tokyo, Japan). Each assay was repeated more than three times to confirm the results. The number of cells was plotted on a time-response curve as indicated in the figures.

Tumor xenograft assay. Male four-week-old BALB/cSlc-nu/nu mice obtained from Japan SLC, Inc. (Shizuoka Japan) were used. M2, M2TRB3 and M2mock cells ($1.0x10^6$/200 μl) were subcutaneously inoculated into the right lower flank of the mice. Tumor diameters (mm) and body weight (g) were recorded twice weekly. The tumor volume (mm^3) was calculated by the formula: Volume = L x D x H x π/6, where L is the length, D is the depth, and H is the height. At 35 days after inoculation, all mice were euthanized and complete autopsies were performed. Animal experiments were conducted in accordance to the regulations specified by the Institutional Animal Use and Care Committee of Nagoya City University.

Immunohistochemistry and measurement of proliferating cell nuclear antigen (PCNA) labeling index. These assays were performed using an established method as described previously by us (16). Paraffin sections (3-μm) were prepared to include tumors resected from the lower flank of each mouse. These sections were treated in 3% H_2O_2 for 10 min to block the endogenous peroxidase activity. For antigen retrieval, the sections were brought to boiling in 0.1 M citrate buffer, pH 6.0. Sections were incubated with a primary antibody of PCNA (1:500 dilution) (sc-56; Santa Cruz Biotechnology, Inc., Santa Cruz, CA, USA) at room temperature for 60 min. After incubation with the secondary antibody, sections were then stained using an ABC kit (Vector Laboratories, Inc., Burlingame, CA, USA) according to the manufacturer's instructions. The PCNA labeling index was determined by calculating the ratio of PCNA-positive nuclei/total number of nuclei counted. Ten high power fields (x400) per tumor were examined, and >300 cells were counted in each tumor. In M2TRB3 and M2mock tumors, the longest diameter of the nucleus was determined by image analysis using Olympus DP70 system (Olympus Corp., Tokyo, Japan). Four high power fields (x400) per tumor were examined and more than 100 nuclei were counted in each tumor.

Flow cytometric analysis. These assays were performed as previously described (16). M2TRB3 and M2mock cells ($7.5x10^4$ cells/plate) were plated onto 9-cm culture dishes in DMEM plus 10% FBS and grown to yield 50-60% confluence. To synchronize cells at the G0/G1 phase, they were starved by culturing in DMEM plus 0.5% FBS for 48 h. After starvation, cells were then growth in DMEM plus 10% FBS for 72 h. Adherent cells were washed twice with PBS, fixed with 5 ml 70% ethanol, centrifuged, resuspended in 400 μl PBS containing 2 mg/ml RNase (Nacalai Tesque, Inc., Kyoto, Japan), and stained with 400 μl of 0.1 mg/ml propidium iodide (Sigma-Aldrich, St. Louis, MO, USA) in the dark for 30 min or overnight. The cell suspension was filtered through a 60-μm nylon filter (Ikemoto Scientific Technology Co., Ltd., Tokyo). Samples of 10,000-20,000 cells were then analyzed for cell cycle phase distribution and ploidy status using a FACSCalibur™ instrument, and the data were analyzed with the CellQuest computer program (both from Becton-Dickinson, Franklin lakes, NJ, USA) as described in a previous study (16). Cells were harvested just after starvation (0 h) and 72 h after starvation as described in Table I and Fig. 5. Each assay was repeated more than three times to confirm the results.

RT-PCR assays. These assays were conducted using previously established procedures (16). Total RNA was extracted from each cell line grown in 9-cm culture dishes using Isogen (Nippon Gene, Toyama, Japan). The reaction mixture contained 4 μg of total RNA, 1 μl of 10 mM dNTP, 1 μl of random primers (both from Life Technologies, Inc.) and 7 μl of distilled water. The reaction mixture was incubated at 65˚C (5 min) for denaturation, chilled on ice for 1 min and 4 μl of 5X RT buffer (Life Technologies, Inc.), 1 μl of 0.1 M dithiothreitol (DTT), 1 μl of the RNaseOut and 1 μl of Superscript® III Reverse Transcriptase (both from Life Technologies, Inc.) were added. After the addition of these reagents, the reaction mixture was incubated at 50˚C (60 min) for random primer annealing and 70˚C (15 min) for cDNA preparation. One microliter of the reaction mixture was then used for PCR. The primer sequences used in this study were as follows: human TRB3-specific

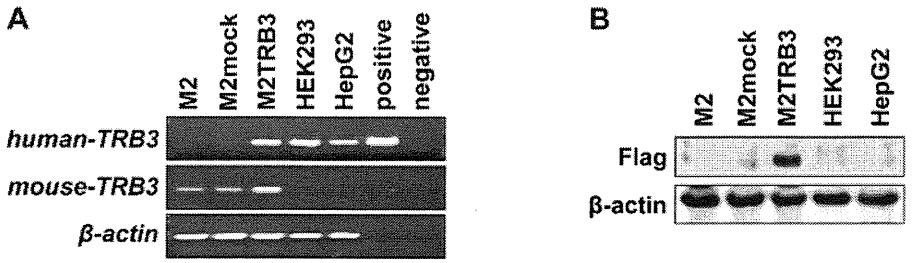

Figure 1. Expression status of exogenous human TRB3 and endogenous mouse TRB3 in the indicated cell lines. (A) Representative results of the RT-PCR analysis. The band in the positive control was derived from DNA fragments that were PCR-amplified using pcDNA3.1-Hygro-flag-human TRB3 vector as a template and the pairs of gene-specific primers listed in Materials and methods. No band was noted in the negative control since the empty vector (pcDNA3.1-Hygro) that does not carry specific sites for the primers was used as a template for PCR. Bands of β-actin were not observed in the positive and negative control samples due to the same reason as the negative control. (B) Representative results of the western blot analysis. The exogenous human TRB3 (Flag) protein was detected in the M2TRB3 cells.

primer set, hTRB3F (5'-CAAGTCGCTCTGAAGGTTCC-3') and hTRB3R (5'-CCATCCTACTCTGGCAAAGC-3'), mouse TRB3-specific primer set, mTRB3F (5'-CAAGTCGCTCT GAAGGTTCC-3') and mTRB3R (5'-CCATCCTACTC TGGCAAAGC-3'), respectively.

β-actin-specific DNA fragments from the same RNA samples were amplified and served as internal controls. Primers actinF (5'-CCGTAAAGACCTCTATGCCAACA-3') and actinR (5'-CGGACTCATCGTACTCCTGCTT-3') were used for amplification of β-actin. PCR was conducted for 26-30 cycles in an iCycler (Bio-Rad Laboratories, Inc., Hercules, CA, USA). Each amplification cycle consisted of 0.5 min at 94°C for denaturation, 0.5 min at 60°C for primer annealing, and 1 min at 72°C for extension. After PCR amplification, the DNA fragments were stained with ethidium bromide and analyzed by 2% agarose gel electrophoresis. The results were confirmed by repeating the experiments.

Western blot assays. These assays were conducted according to previously established procedures (17). The cells were lysed in radioimmunoprecipitation assay (RIPA) buffer [50 mM Tris-HCl (pH 8.0), 150 mM NaCl, 0.1% sodium dodecyl sulfate (SDS), 0.5% deoxycholate, and 1% Triton X-100]. The lysates were subjected to SDS-polyacrylamide gel electrophoresis (PAGE) (12.5%), transferred onto a polyvinylidene difluoride (PVDF) membrane (Immobilon P; Millipore Corp., Bedford, MA, USA) and probed with the antibodies. The primary antibodies used in the present study were anti-β-actin monoclonal antibody (AC-15) (Sigma-Aldrich), anti-cyclin B1 monoclonal antibody (sc-245) (Santa Cruz Biotechnology Inc.), anti-Cdc2 monoclonal antibody (sc-54), anti-Cdk2 polyclonal antibody (sc-163), anti-Cdk4 polyclonal antibody (sc-260), anti-TRB3 polyclonal antibody (sc-34211), anti-cyclin D1 monoclonal antibody (556470; Becton-Dickinson), and anti-Flag monoclonal antibody (018-22381) (Wako Pure Chemical Industries, Ltd.). The immunoreactive proteins were visualized using ImmunoStar Zeta (Wako Pure Chemical Industries, Ltd.) and light emission was quantified with Light Capture (ATTO Corp., Tokyo, Japan). Each assay was repeated more than three times to confirm the results.

Statistical analysis. Differences in the number of cells, tumor volume, PCNA labeling index, and rate of DNA ploidy between cell lines or tumor origins were analyzed by the Student's or Welch's t-test. A value of $P<0.05$ was considered to indicate a statistically significant result.

Results

TRB3 expression in the M2TRB3 cells. To examine the role of TRB3 in cell proliferation, we developed a cell line (M2TRB3) that stably expresses the human *TRB3* gene by transfecting the gene into murine mammary tumor cell line Cl66M2 (M2) (18). We also developed the control cells (M2mock) transfected with empty vector pcDNA3.1-Hygro. M2TRB3 cells expressed both human *TRB3* mRNA and mouse *TRB3* mRNA (Fig. 1A). Human embryonic kidney cell line HEK293 and human hepatoma cell line HepG2 also expressed human *TRB3* mRNA. There was no mRNA expression of human TRB3 in the M2 and M2mock cells. Human TRB3 DNA was PCR-amplified from pcDNA3.1-Hygro-flag-human TRB3 vector and the band was present in the positive lane in Fig. 1A. Expression of the exogenous TRB3 protein (Flag) was present in the M2TRB3 cells. No expression was noted in the protein samples derived from M2, M2mock, HEK293 and HepG2 cells (Fig. 1B). The M2TRB3 and M2mock cells were used for cell proliferation assays.

TRB3 gene enhances cell proliferation and tumor volume. To examine the tumorigenic activity of the TRB3 gene, we investigated its effects on cell and tumor growth using M2TRB3 and M2mock cells. The number of M2TRB3 cells significantly increased compared to M2mock cells at the 48 and 72 h time points ($P<0.01$ and 0.05, respectively) (Fig. 2A). At 72 h, a 34% increase was noted in the number of M2TRB3 cells compared to that of the M2mock cells. To examine the extent of M2TRB3 cell growth when these cells were implanted into the subcutaneous tissue of mice, we used the xenograft mouse model as described in Materials and methods. Twice a week observation was carried out with all mice throughout the experiment. Tumor growth was monitored with the naked eye from day 7 to 35 after inoculation; tumor volume (mm^3) and body weight (g) were measured twice weekly. No specific physical and behavioral changes were noted in any mice. The average volume of the tumors derived from the M2TRB3 cells was significantly increased by 38% when compared with that of the M2mock tumors at experimental day 35 ($P<0.05$) (Fig. 2B).

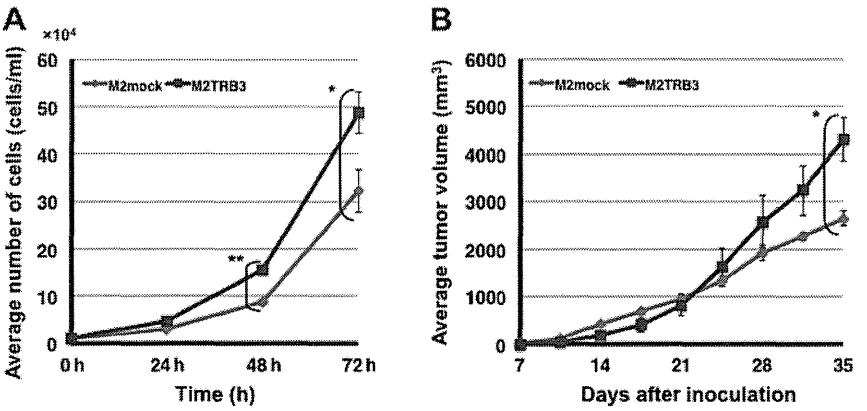

Figure 2. Growth enhancing effects of the TRB3 gene. (A) Growth curve of the cell proliferation assay. Asterisk(s) indicate statistical significance between the two cell lines (*P<0.05, **P<0.01). (B) Volume of the M2TRB3 tumors and M2mock tumors. Asterisk indicates statistical significance in tumor volume between the two tumors (*P<0.05).

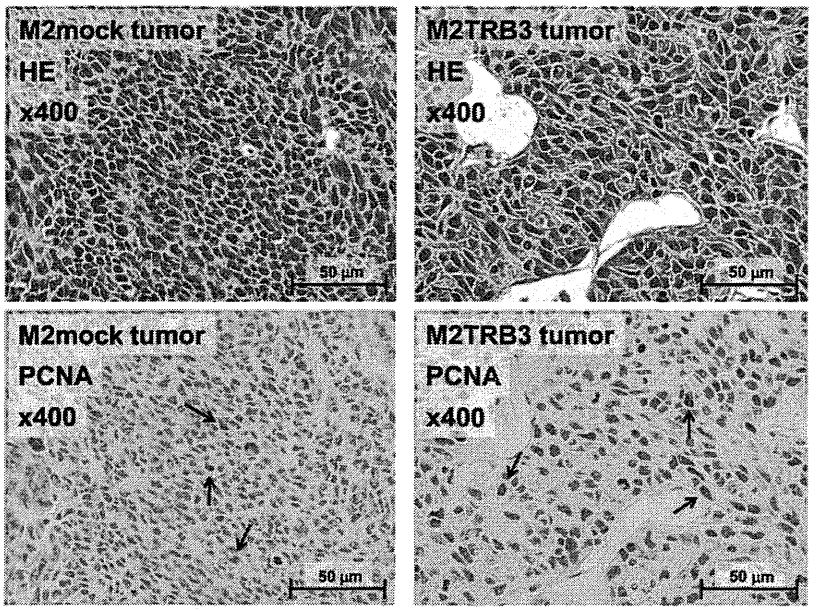

Figure 3. Representative histological features of the M2mock (left rows) and M2TRB3 tumors (right rows). Upper panels were stained with hematoxylin and eosin (HE) and lower panels show immunohistochemical staining of proliferating cell nuclear antigen (PCNA). Approximately 20 and 35% of M2mock and M2TRB3 cells were PCNA-positive (arrows), respectively. Magnification was x400 in all four images.

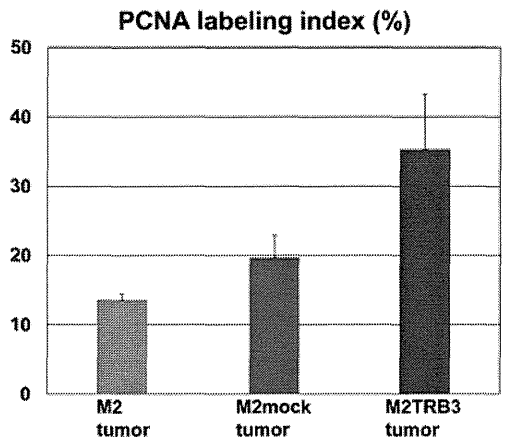

Figure 4. PCNA labeling index in the M2, M2mock and M2TRB tumors. A marked difference was noted between M2mock and M2TRB3 tumors but this difference did not achieve statistical significance.

Gross and histological features and PCNA labeling index of the M2TRB3 tumors. Due to the growth enhancing effects identified above, we aimed to determine whether the TRB3 gene induced morphological changes in tumor tissues. The M2TRB3, M2mock and M2 tumors were excised from the mouse skin, fixed with 10% buffered formalin, and stained with hematoxylin and eosin for histological examination. The tumors were analyzed using a light microscope. M2TRB3 and M2mock tumors presented a pedunculated round shape. Histologically, M2mock tumor cells grew in a solid appearance (Fig. 3, left upper panel). A site of necrosis was present in the central region of the tumor. M2TRB3 tumors were also solid and papillary growth was partially noted (Fig. 3, right upper panel). In the M2TRB3 tumors, the mean diameter of the nucleus (9.4±0.3 μm) was significantly greater than that (7.0±0.2 μm) of the M2mock tumors (P<0.001). The cell proliferation rate was evaluated by measuring the PCNA